

Research Paper

Liquefaction-induced large deformation method with automatic time-step mapping and interfacial interpolation improvement: Case study of the San Fernando dam

Jin Gong^{a,b}, Degao Zou^{a,b,*}, Xianjing Kong^{a,b}, Jingmao Liu^{a,b}, Kai Chen^{a,b}, Yongqian Qu^{a,b}, Xiang Yu^c

^a The State Key Laboratory of Coastal and Offshore Engineering, Dalian University of Technology, Dalian, Liaoning 116024, China

^b School of Hydraulic Engineering, Dalian University of Technology, Dalian, Liaoning 116024, China

^c School of Water Conservancy Engineering, Zhengzhou University, Zhengzhou, Henan 450001, China

ARTICLE INFO

Keywords:

Liquefaction-induced large deformation
Meshfree method
Saturated soil
Radical basis function
San Fernando dam

ABSTRACT

This study constructed the u - p equation for saturated soil in the meshfree global weak form within the arbitrary Lagrangian-Eulerian (ALE) framework to solve the problem of liquefaction-induced large deformation induced by strong seismic loading. The interpolation improvement in the near-interface zone was achieved using domain truncation optimization and the local nodal refinement algorithm, and the relative error of the shape function was proposed as the judgment criterion for radial basis function (RBF) field variable mapping. Finally, a high precision meshfree liquefaction-induced large deformation method (MFLDLM) with automatic time step mapping and interfacial zone interpolation improvement was established. The MFLDLM achieved the efficient dynamic updating of soil stress state and pore pressure information in space during the deformation process and more accurately depicted the localized large shear deformation characteristics of the soil in the near-interface zone. The proposed method was integrated into a custom-built large-scale finite element method (FEM) computing system (GEODYNA), based on object-oriented and super element program design technology. This enabled the efficient coupled analysis of MFLDLM in the liquefied-induced large deformation zone and FEM in the small deformation zone. Numerical consolidation examples were used to validate the accuracy, convergence, and applicability of the soil elasto-plastic model for MFLDLM. The method was then used to simulate the liquefaction damage of the San Fernando dam, which reproduced the development process of large slip deformation and high-water pressure ratio for the upstream dam slope.

1. Introduction

As a typical saturated porous medium, soil undergoes rapid and severe shear deformation under the influence of strong seismic load, resulting in a rapid increase in excess pore water pressure (EPWP) and a decrease or even elimination of effective stress in the soil skeleton. This can cause liquefaction-induced large-deformation phenomena of saturated soil (Shahbodagh et al., 2020; Hatanaka et al., 1997; Gu et al., 1993), such as foundation settlement, slope instability, and liquefaction of the dam slide, which pose a serious threat to the safe operation of structures. Numerous powerful earthquakes worldwide have resulted in a significant number of soil-liquefaction-induced large deformation phenomena and structural damage, including the 1964 Niigata

earthquake in Japan, the 2008 Wenchuan earthquake, and the 2010 Chile earthquake. In geotechnical engineering, developing an efficient numerical analysis method to reproduce the soil liquefaction-induced large deformation process is of great theoretical and practical importance (Lombardi and Bhattacharya, 2014; Chen et al., 2023a), to reveal its evolution mechanisms and to evaluate the extent of the liquefaction zone.

Research on soil liquefaction can be divided into two categories, strength-based and deformation-based research. The strength-based approach focuses on the liquefaction discrimination problem (Seed and Idriss, 1971). However, with a deeper understanding of liquefaction damage, studies have shown that deformation will significantly influence the safety of soil and structures, rather than strength, making it

* Corresponding author.

E-mail address: zoudegao@dlut.edu.cn (D. Zou).

<https://doi.org/10.1016/j.compgeo.2024.106351>

Received 17 October 2023; Received in revised form 15 April 2024; Accepted 16 April 2024

Available online 26 April 2024

0266-352X/© 2024 Elsevier Ltd. All rights reserved.

challenging for a single strength-based approach to meet a project's requirements. Therefore, research focus on soil liquefaction has gradually shifted toward analyzing deformation produced by liquefaction (Liu et al., 2021; Ye and Wang, 2015). The small deformation analysis based on the finite element method (FEM) has failed to account for changes in geometric modeling, making it difficult to accurately capture the development process of large deformation phenomena (Wang et al., 2015; Chen et al., 2023b; Zhao et al., 2024). Using FEM within the updated Lagrangian (UL) or total Lagrangian (TL) (Bathe et al., 1975) framework may offer a strategy for addressing the finite deformation problem. However, this approach may cause severe mesh distortion in large deformation analysis, causing negative value of the Jacobian matrix and computational non-convergence. As a result, pure Lagrangian or Eulerian frameworks have been supplanted with the arbitrary Lagrangian-Eulerian (ALE) framework. Due to its high precision and stability, the ALE framework has been extensively used in large deformation analysis (Chen et al., 2023a; Liu et al., 2022; Gong et al., 2023). Mesh-based and node-based methods comprise major portions of existing large deformation techniques (Wang et al., 2015).

The re-meshing and interpolation technique with small strain (RITSS) (Hu and Randolph, 1998) and coupled Eulerian-Lagrangian (CEL) (Noh, 1963) method serve as two typical mesh-based large deformation methods in the ALE framework. Based on standard FEM small deformation analysis, Hu and Randolph (1998) first proposed the RITSS, which successfully solved the large deformation problem and was extended to dynamic analysis by Wang et al. (2013) and saturated porous media effective stress analysis by Randolph (2008) and Ullah et al., (2018). Seismic liquefaction analysis necessitates a relatively short time interval and a greater number of computational steps, which also requires more frequent re-meshing for the RITSS approach. However, this process can be time-consuming. Additionally, the nodal pore pressure exhibits sensitivity in numerical analysis, thus, more frequent interpolation can impact its simulation precision. The CEL method can convert Lagrangian control equations into Eulerian control equations and maintain the original mesh throughout the analysis process, allowing for the solution of large deformation problems. The CEL approach was integrated into Abaqus within the total stress analysis framework. Thus, this method did not adequately account for the effects of pore pressure changes and was not appropriate for addressing liquefaction issues. Yi et al. (2021) extended the CEL method to an effective stress framework for dynamic analysis of saturated soil. However, the above secondary development in Abaqus has not been utilized for analyzing liquefaction-induced large deformation analysis under seismic load. Liu et al. (2022) and Chen et al. (2022) combined the CEL approach and random field theory for modeling landslide runout in non-uniform soils. Meanwhile, two recent reviews (Wang et al., 2015; Augarde et al., 2021) analyzed large deformations in geotechnical engineering, however, the application of RITSS and CEL in analyzing soil liquefaction-induced large deformations under seismic load was not discussed. Other mesh-based large deformation methods including: particle finite element method (PFEM) (Idelsohn et al., 2004), efficient arbitrary Lagrangian-Eulerian (EALE) method (Benson, 1989), also have been applied to geotechnical engineering large deformation analysis (Yuan et al., 2020; Zhang et al., 2023c).

With the development of above methods, another class of node-based large deformation analysis methods has also significantly advanced, with the most representative consisting of the meshfree method (MFM) (Lucy, 1977; Belytschko et al., 1994; Liu and Gu, 2001) and the material point method (MPM) (Sulsky et al., 1994). Compared to FEM, MFMs have the advantage of eliminating mesh constraints in the interpolation or numerical integration process, which can avoid the issue of mesh distortion in large deformation analysis. Liu and Gu (2002) provided a definition for the meshfree method as an approach that does not rely on predetermined mesh information during numerical integration or the calculation of the shape function. The existing meshfree methods can be divided into three main categories: 1. The first category is based on the

strong form, and includes the smoothed particle hydrodynamics (SPH) method, which is a completely meshfree method in which the processes of numerical integration and calculating the shape function did not depend on the mesh (Lucy, 1977); 2. The second method is based on the global weak form, and includes the element-free Galerkin method (EFGM) and radial point interpolation method (RPIM), both of which rely on a global background mesh for numerical integration (Belytschko et al., 1994); 3. The third method is based on a local weak form, and includes the meshfree local Petrov-Galerkin method (MLPGM) and local point interpolation method (LPIM), both of which require a local background mesh for numerical integration (Liu and Gu, 2001). Numerous studies (Jie et al., 2008; Huang et al., 2008) have effectively used MFMs to examine the development of structural damage caused by soil liquefaction-induced large deformation under seismic load. However, the applicability of MFMs will be constrained by their relatively low computational efficiency. MPM employs a double description with Lagrangian material points and a Eulerian mesh and discretizes the continuum model into a series of material points; it has been used to successfully simulate the liquefaction-induced large deformation problems for embankments, dams, and landslides (Di Carluccio et al., 2023; Li et al., 2021; Feng et al., 2021; Cuomo et al., 2019; Yerro et al., 2019; Bandara et al., 2016). Different from FEM, MPM established discrete governing equations using material points instead of a mesh, and it required information transmission between the material points and background mesh nodes. Therefore, integrating MPM with commercial or self-developed FEM programs may be challenging. Additional information regarding the aforementioned node-based methods can be found in the literatures (Liew et al., 2002; Guo et al., 2021).

Based on the benefits and limitations of the above-presented approaches, this study introduced an efficient and practicable meshfree liquefaction-induced large deformation method (MFLDLM) with following contributions: (1) Develop an effective stress-pore water pressure large deformation analysis with the advantages of MFM and ALE. (2) The relative error of shape function was proposed as the mapping judgment criterion, which achieves automatic time-step mapping. (3) The interpolation improvement in the near-interface zone was achieved to accurately capture the localized behaviors of the near-interfacial soils.

The accuracy and convergence of proposed MFLDLM is verified by simulating the consolidation problem of saturated soil columns, transient response problem in a saturated elastic half space and simulation of centrifuge test. Then, the generalized elasto-plastic model (Liu et al., 2018; Zienkiewicz et al., 1985) was employed in MFLDLM to accurately capture the cyclic shear deformation and post-seismic permanent deformation of soil under seismic loading. This constitutive model was finally applied to simulate the liquefaction damage of the San Fernando Dam. The numerical analysis reproduced the liquefaction-induced large deformation of the upstream slope during powerful earthquakes and identified the region of high excess pore water pressure ratio of the dam.

2. Formula derivation in MFLDLM

The proposed MFLDLM required a global background mesh in numerical integration, but it calculated the shape function only using the nodal information. Consequently, according to the aforementioned definition given by Liu and Gu (2002), it could be classified as a meshfree approach. Section 2.1 provides the derivation of the governing equation of MFLDLM in both Lagrangian step and Eulerian step; Section 2.2 summarizes the automatic time-step mapping technology; Section 2.3 describes the enhancement of calculating the shape function near the interface zone between two materials; and Section 2.4 gives the improvement of calculating lumped mass matrix to solve the problem of calculation divergence.

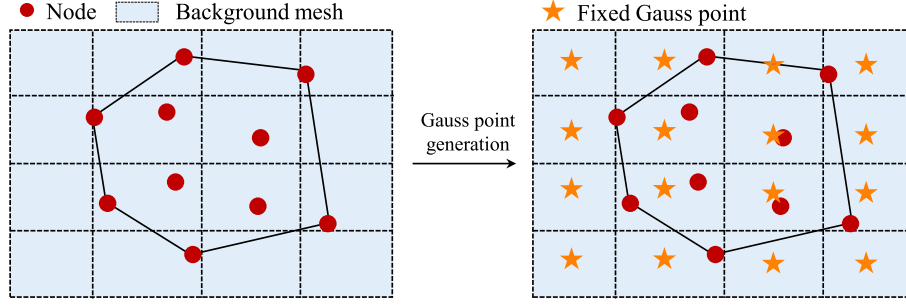


Fig. 1. Schematic of the fixed Gauss points on the basis of the background mesh.

2.1. Derivation of u - p equations

The proposed MFLDM was established within the arbitrary Lagrangian-Eulerian (ALE) framework, and every calculation step in MFLDM involved both a Lagrangian step and a Eulerian step. In the Lagrangian step, the standard governing equations in the small deformation condition were established. Biot's dynamic consolidation theory was first proposed in 1956, and it has been extensively applied to dynamic problems involving saturated porous media. The researchers deduced several forms of these equations, with the u - p form equations selected as the governing equations in this work.

The solid's equilibrium equations can be expressed as follows:

$$\mathbf{L}^T \boldsymbol{\sigma} - \rho \ddot{\mathbf{u}} + \rho \mathbf{b} = \mathbf{0} \quad \mathbf{L}^T (\boldsymbol{\sigma}' - m\mathbf{p}) - \rho \ddot{\mathbf{u}} + \rho \mathbf{b} = \mathbf{0} \quad (1)$$

where $\boldsymbol{\sigma}$ and $\boldsymbol{\sigma}'$ denote the total stress vector and effective stress vectors, respectively, p is the pore water pressure, m can be expressed as $\{1, 1, 0\}^T$, ρ is the density of the solid, \mathbf{b} is the solid load vector, $\ddot{\mathbf{u}}$ is the acceleration vector of the solid skeleton, and the differential operator \mathbf{L} can be calculated as follows:

$$\mathbf{L} = \begin{bmatrix} \frac{\partial}{\partial x} & \frac{\partial}{\partial y} \\ \frac{\partial}{\partial y} & \frac{\partial}{\partial x} \end{bmatrix} \quad (2)$$

The equilibrium equations of the fluid can be expressed as follows:

$$-\nabla p - \mathbf{R} - \rho_f \ddot{\mathbf{u}} + \rho_f \mathbf{b}_f = \mathbf{0} \quad (3)$$

where \mathbf{R} represents the viscous drag force vector, ρ_f is the density of the fluid, and \mathbf{b}_f is the fluid load vector. The gradient operator ∇ can be expressed as follows:

$$\nabla = \left\{ \frac{\partial}{\partial x} \quad \frac{\partial}{\partial y} \right\}^T \quad (4)$$

According to Darcy's law,

$$\mathbf{k}\mathbf{R} = \mathbf{w} \quad (5)$$

where \mathbf{k} is the permeability and \mathbf{w} is the average velocity vector of the percolating fluid.

The continuity equation can be expressed by:

$$\nabla^T \mathbf{w} + \nabla^T \dot{\mathbf{u}} + \frac{\dot{p}}{Q} = 0 \quad (6)$$

where \dot{p} signifies the derivative of pore water pressure according to the time, and Q is the modulus parameter defined as:

$$\frac{1}{Q} = \frac{n}{K_f} + \frac{1-n}{K_s} \quad (7)$$

where n represents the porosity of soil, K_f and K_s are the bulk modulus of the fluid and solid, respectively.

Finally, Equation (6) can be re-expressed as follows:

$$-\nabla^T \mathbf{k} \nabla p - \rho_f \nabla^T \ddot{\mathbf{u}} + \rho_f \nabla^T \mathbf{b}_f + \alpha \nabla^T \dot{\mathbf{u}} + \frac{\dot{p}}{Q} = 0 \quad (8)$$

where α represents the parameter related to the bulk modulus ratio of the solid skeleton and the solid particle; in this manuscript $\alpha=1$.

The equilibrium equation (Equation (1)) and continuity equation (Equation (8)) consist of the u - p form of Biot's dynamic consolidation for saturated porous media. Using the virtual displacement principle, the weak forms of the equilibrium equation and continuity equation can be expressed as follows:

$$\mathbf{M} \ddot{\mathbf{u}} + \mathbf{C} \dot{\mathbf{u}} + \mathbf{K} \mathbf{u} - \mathbf{Q}_s \bar{p} - \mathbf{f}^1 = \mathbf{0} \quad (9)$$

$$\mathbf{Q}_s \dot{\mathbf{u}} + \mathbf{S} \bar{p} + \mathbf{H} \bar{p} - \mathbf{f}^2 = \mathbf{0} \quad (10)$$

where \mathbf{f}^1 is the nodal external load vector corresponding to the solid, and \mathbf{f}^2 is the nodal external load vector corresponding to the fluid.

To calculate the corresponding matrices and vectors in the preceding equations, interpolation and integration processes had to be performed. Unlike FEM, the background mesh was introduced to support the aforementioned processes. The background mesh was requested to cover the entire domain, and it remained unaltered throughout the simulation. This study employed the rectangular background mesh to simplify the calculation, with its dimensions l_x and l_y related to the average nodal distance:

$$l_x = l_y = \frac{1}{num} \sum_{i=1}^{num} r_i \quad r_i = \frac{1}{num-1} \sum_{j=1, j \neq i}^{num} \sqrt{(x_i - x_j)^2 + (y_i - y_j)^2} \quad (11)$$

where num represents the number of nodes within the analyzed model, where for the i th node, the r_i was the average distance between itself and other nodes through coordinates (x_i, y_i) and (x_j, y_j) .

A set of Gauss points was constructed within the background mesh. In this study, 2×2 Gauss points were set in each background mesh, and their coordinates $(x_{gi,k}, y_{gi,k})$ (k represents the k th background mesh) could be calculated with the background mesh's coordinates $(x_{bi,k}, y_{bi,k})$. The above Gauss point was fixed to the background mesh, and its location remained constant throughout the analysis; hence, it was referred to as the fixed Gauss point. The fixed Gauss points were utilized for interpolation, integration, and establishing equation processes. Fig. 1 depicts a schematic of the background mesh and fixed Gauss point.

In contrast to FEM, a portion of the fixed Gauss points was positioned outside the analyzed model and did not contribute to matrix and vector. The shape function of the Gauss points inside the model could be calculated through the nodes within its supporting domain. The distance between the i th fixed Gauss point and the m th node was calculated, and if the distance was less than the supporting domain radius d_i of the i th fixed Gauss point, we concluded that the m th node was set inside the supporting domain of the i th Gauss point, according to

$$\sqrt{(x_{gi,k} - x_i)^2 + (y_{gi,k} - y_i)^2} \leq d_i \times r_{mi} \quad (12)$$

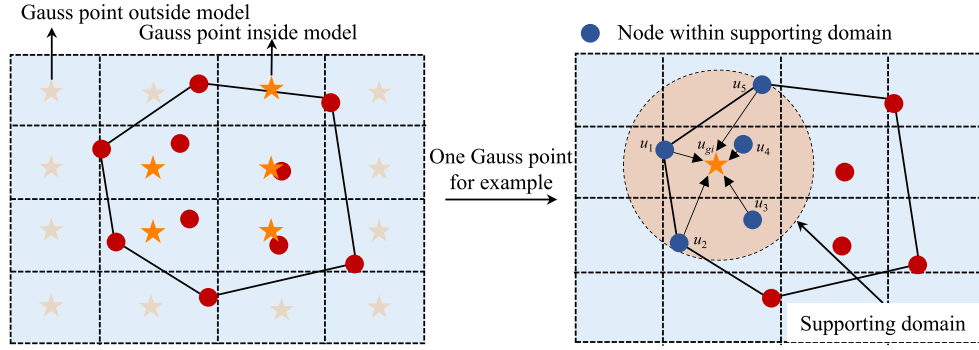


Fig. 2. The nodes within the supporting domain of a fixed Gauss point.

$$r_{mi} = \{r(x_i, x_1), \dots, r(x_i, x_{num})\}_{min} \quad r(x_i, x_j) = \sqrt{(x_i - x_j)^2 + (y_i - y_j)^2} \quad i \neq j \quad (13)$$

where $alfs$ represents the coefficient of the supporting domain; in this work, $alfs$ equals 3, according to the findings of Liu and Gu (2001). The impact of $alfs$ values on the precision of MFLDLM will be discussed in a subsequent section. Fig. 2 shows the nodes within the supporting domain of a fixed Gauss point.

The displacement vector of each fixed Gauss point could be expressed by the nodes within its supporting domain:

$$u(x) = \sum_{i=1}^{num} R(r) a_i + \sum_{j=1}^m p(x) b_j \quad (14)$$

where a_i and b_j are constants to be solved in the RBF shape function, r is the distance vector between a node and a fixed Gauss point, and num is the number of nodes within the supporting domain.

$R(r)$ served as the radial basis matrix, and the contents of the matrix in the i th row and j th column could be calculated as follows:

$$R(r)_{ij} = (r_{ij} + cd_{av})^q \quad (15)$$

where d_{av} is the average nodal distance, r_{ij} denotes the distance between the i th and j th nodes, c and q are constant parameters, with $c = 3$, $q = 1.03$ based on the values obtained from research conducted by Liu and Gu (2001). The impact of these parameter values on the precision of MFLDLM will also be examined through a subsequent numerical example. The multi-quadric (MQ) radial basis was adopted in this work, with $p(x)$ being the additional linear bases vector, and $m = 3$. The linear bases vector was $[1 \ x \ y]$.

To calculate the shape function, the following equation in matrix form was established:

$$\begin{bmatrix} u \\ 0 \end{bmatrix} = \begin{bmatrix} R(r) & p(x) \\ p^T(x) & 0 \end{bmatrix} \times \begin{bmatrix} A \\ B \end{bmatrix} \quad (16)$$

The matrices in the above equation could be expressed as follows:

$$R(r)^T = \begin{bmatrix} R(r_{11}) & R(r_{12}) & \dots & R(r_{1num}) \\ R(r_{21}) & R(r_{22}) & \dots & R(r_{2num}) \\ \dots & \dots & \dots & \dots \\ R(r_{num1}) & R(r_{num2}) & \dots & R(r_{numnum}) \end{bmatrix} \quad (17)$$

$$p(x)^T = \begin{bmatrix} 1 & 1 & \dots & 1 \\ x_1 & x_2 & \dots & x_{num} \\ y_1 & y_2 & \dots & y_{num} \end{bmatrix} \quad (18)$$

$$[A \ B]^T = [a_1 \ a_2 \ \dots \ a_{num} \ b_1 \ b_2 \ b_3] \quad (19)$$

After solving the above equations, the constant matrices A and B could be expressed as follows:

$$A = S_a u_e = R^{-1}(r) [I - p(x) S_a] u_e \quad (20)$$

$$B = S_b u_e = [p^T(x) R^{-1}(r) p(x)]^{-1} p^T(x) R^{-1}(r) u_e \quad (21)$$

where u_e is the vector of nodal displacements and I is the unit matrix.

Subsequently, the shape functions could be expressed as follows:

$$u(x) = [R^T(r) S_a + p^T(x) S_b] u_e = \phi_u u_e = \{\phi_1 \ \phi_2 \ \dots \ \phi_{num}\} u_e \quad (22)$$

where ϕ_u is the shape function vector of a selected fixed Gauss point, with its dimension equal to the number of nodes within its supporting domain. In this work, the displacement shape functions ϕ_u were equal to the pore pressure shape functions ϕ_p .

The matrix and vector in Equations (9) and (10) could be calculated as follows. The Rayleigh damping was adopted to calculate the damping matrix in this manuscript. Although the elasto-plastic constitutive model was employed to represent soil damping in Section 4.3 and Section 5, a certain amount of Rayleigh damping was also applied to enhance stability for dynamic analysis.

$$K = \iint_{\Omega} B^T D B d\Omega \quad (23)$$

$$M = \iint_{\Omega} N^T \rho N d\Omega \quad (24)$$

$$C = \alpha M + \beta K \quad (25)$$

$$H = \iint_{\Omega} \bar{B}^T k \bar{B} d\Omega \quad (26)$$

$$S = \iint_{\Omega} N^T \frac{1}{Q} N d\Omega \quad (27)$$

$$Q_{fs} = \iint_{\Omega} \bar{N}^T m^T B d\Omega = Q_{sf}^T \quad (28)$$

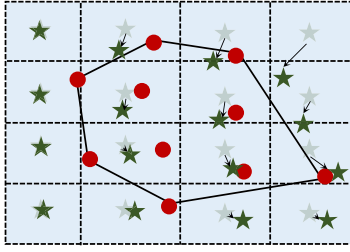
$$F_1 = F^b + F^t = \int_{\Gamma} N^T f_t d\Gamma + \iint_{\Omega} N^T f_b d\Omega \quad (29)$$

$$F_2 = \int_{\Gamma} N^T v_n d\Gamma + \iint_{\Omega} B^T k f_b d\Omega \quad (30)$$

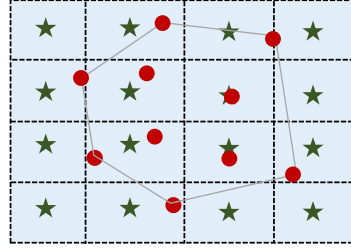
where

$$N = \begin{bmatrix} \phi_1 & 0 & \dots & \phi_{num} & 0 \\ 0 & \phi_1 & \dots & 0 & \phi_{num} \end{bmatrix} \quad \bar{N} = [\phi_1 \ \phi_2 \ \dots \ \phi_{num}] \quad (31)$$

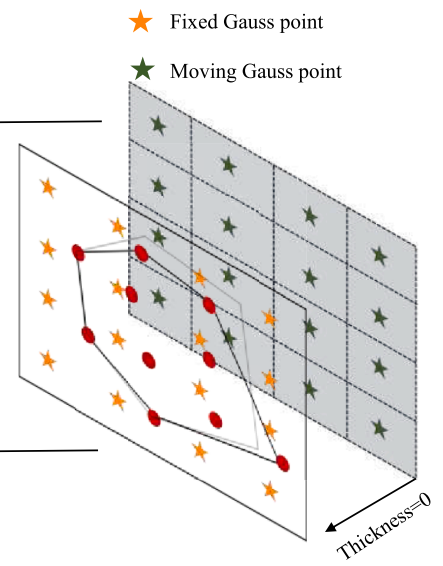
Coordinates of moving Gauss point change with nodes



Deformed model



Original model



Coordinates of fixed Gauss point don not change

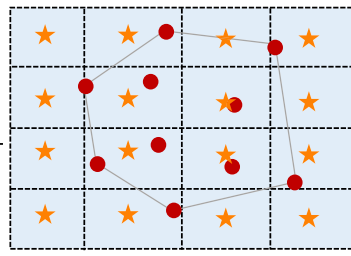
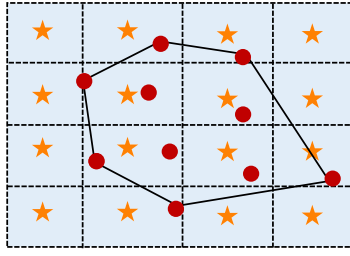


Fig. 3. The updated coordinate of moving Gauss point according to nodal displacement.

$$\mathbf{B} = \begin{bmatrix} \frac{\partial \phi_1}{\partial x} & 0 & \dots & \frac{\partial \phi_{num}}{\partial x} & 0 \\ 0 & \frac{\partial \phi_1}{\partial y} & \dots & 0 & \frac{\partial \phi_{num}}{\partial y} \\ \frac{\partial \phi_1}{\partial y} & \frac{\partial \phi_1}{\partial x} & \dots & \frac{\partial \phi_{num}}{\partial y} & \frac{\partial \phi_{num}}{\partial x} \end{bmatrix} \quad \bar{\mathbf{B}} = \begin{bmatrix} \frac{\partial \phi_1}{\partial x} & \frac{\partial \phi_2}{\partial x} & \dots & \frac{\partial \phi_{num}}{\partial x} \\ \frac{\partial \phi_1}{\partial y} & \frac{\partial \phi_2}{\partial y} & \dots & \frac{\partial \phi_{num}}{\partial y} \end{bmatrix} \quad (32)$$

By solving the above equations under small deformation framework, the nodal information (displacement, pore pressure, velocity, and acceleration) and the Gauss point information (stress, strain, and constitutive values) could be obtained. Then the Eulerian step was conducted, and the nodal coordinates were updated with the nodal displacement with Equation (33).

$$(x_i, y_i)' = (x_i, y_i) + (u_{i,x}, u_{i,y}) \quad (33)$$

where the superscript denotes the model state after deformation, and $(u_{i,x}, u_{i,y})$ denotes the solved nodal displacement in the Lagrangian step.

The coordinates of the fixed Gauss points remained unaltered throughout the analysis, and the Gauss point field variables could not be redistributed during large deformation. Consequently, another set of moving Gauss points was established within the same background mesh, and the moving Gauss points shared the same coordinate and field

variable information as the fixed Gauss points. As shown in Fig. 3, the coordinates of the moving Gauss point changed with nodal displacement through RBF:

$$(x_{gi,k}, y_{gi,k})' = (x_{gi,k}, y_{gi,k}) + \{\phi_1' \quad \phi_2' \quad \dots \quad \phi_{num}'\} (u_{i,x}, u_{i,y}) \quad (34)$$

where ϕ_i' is the value of the mapping function based on RBF between the moving Gauss points and nodes, and its calculation process was the same as ϕ_i in Equations (14) – (22). Because the moving Gauss point shared the same coordinate with the fixed Gauss point, the value of ϕ_i' was equal to the value of ϕ_i .

Because the moving Gauss point coordinates already changed, integration was no longer appropriate. The fixed Gauss point did not consider the redistribution of field variable information and was also unsuitable for integration. Thus, two different types of field variables information (including: stress, strain, constitutive model variables) transmission techniques (between moving and fixed Gauss points) for MFLDM are provided. The stress, strain, and constitutive model variables of moving Gauss points after deformation are calculated using an RBF-based mapping technique, as depicted in Fig. 4. The mapping equations are given in equations (35) and (36).

$$(\sigma_i, \epsilon_i)' = \{\phi_{g1}' \quad \phi_{g2}' \quad \dots \quad \phi_{gnum}'\} [(\sigma_i, \epsilon_i) + \Delta(\sigma_i, \epsilon_i)] \quad (35)$$

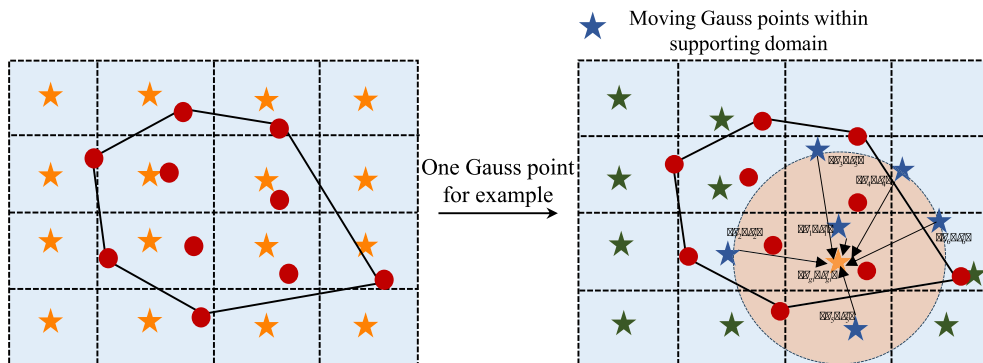


Fig. 4. Field variable information mapping from the moving Gauss points to the fixed Gauss points.

$$\kappa'_i = \{ \phi'_{g1} \quad \phi'_{g2} \quad \dots \quad \phi'_{gnum} \} \kappa_i \quad (36)$$

where $(\sigma_i, \varepsilon_i)$ and $\Delta(\sigma_i, \varepsilon_i)$ are the current and increased stress and the strain of fixed Gauss points, respectively, κ represents the constitutive model variables vector, $(\sigma_i, \varepsilon_i)'$ and κ' are the field variable information of moving Gauss points after deformation, and ϕ_{gi} is the mapping function between the moving Gauss points and fixed Gauss points, with a similar calculation process as ϕ_i .

The constitutive model variables of Gauss points are directly related to their stress and strain, the mapping process described in equation (36) fails to reflect this relationship effectively. As a result, type 1 was unable to ensure the consistency condition at the Gauss points throughout the deformation. In type 2, the calculation process of stress and strain at moving Gauss points is consistent with type 1 (equation (35)). However, the constitutive model variables for moving Gauss points are determined by the mapped stress, mapped strain of moving Gauss points, and constitutive model variables of fixed Gauss points (which contain information on stress histories), as shown in equation (37). In contrast to equation (36), equation (37) considers the correlation among the field variables information and can guarantee the consistency condition of the Gauss points.

$$\kappa'_i = f(\sigma'_i, \varepsilon'_i, \kappa_i) \quad (37)$$

However, in this method, a 5 % shape function relative error value was established as the mapping criterion (conducting in the following section), the non-consistency error in the mapping process of this method was controlled and the computational precision could also be guaranteed. To further substantiate this conclusion, we conducted a comparative analysis of the shear stress time history curve of a Gauss point under seismic load in Section 5 (type 1 vs. type 2).

Mentionable, due to the error caused by the mapping process (Bardenhagen, 2002) of the field variable information (strains, stresses, and field variables) between moving and fixed Gaussian points, the proposed method suffered from energy dissipation (Kafaji, 2013, Martinelli and Galavi, 2022). However, in this method, a relatively brief time interval (for implicit analysis) was utilized. Meanwhile, the mapping error was considered an unbalanced force in the subsequent calculation step for iteration, as shown in Equations (38), where f_{un}^1, f_{un}^2 is the unbalanced nodal external load vector corresponding to the solid or fluid in previous calculation step. As a result, the energy dissipation was controlled within a certain range, ensuring the accuracy of the simulation.

$$M\ddot{u} + C\dot{u} + Ku - Q_{sf}\bar{p} - f^1 - f_{un}^1 = 0 \quad Q_{fs}\ddot{u} + S\dot{p} + H\bar{p} - f^2 - f_{un}^2 = 0 \quad (38)$$

Following the mapping process, the moving Gauss point was restored to its initial coordinates for the subsequent calculation step. In conclusion, the information regarding displacement, velocity, acceleration, and pore pressure was re-distributed with the nodes during large deformation analysis. Meanwhile, the stress, strain, and constitutive values were re-distributed with the Gauss point using RBF-based mapping technology. The above processes demonstrated that the proposed method could be effectively applied to solve liquefaction-induced large deformation problems.

2.2. Automatic time-step mapping

In dynamic analysis, the equations had to be discretized in time, and the generalized Newmark method (Newmark, 1959) was adopted. The relationship between time t and $t + \Delta t$ is given by

$$\begin{aligned} \ddot{u}_{t+1} &= \ddot{u}_t + \Delta\ddot{u}_t \quad \dot{u}_{t+1} = \dot{u}_t + \ddot{u}_t\Delta t + \beta_1\Delta\ddot{u}_t\Delta t \\ &= \ddot{u}_t + \dot{u}_t\Delta t + \frac{1}{2}\ddot{u}_t\Delta t^2 + \frac{1}{2}\beta_2\Delta\ddot{u}_t\Delta t^2 \end{aligned} \quad (39)$$

$$\dot{p}_{t+1} = \dot{p}_t + \Delta\dot{p}_t \quad \bar{p}_{t+1} = \bar{p}_t + \dot{p}_t\Delta t + \beta_1\Delta\dot{p}_t\Delta t \quad (40)$$

To ensure the accuracy and convergence of dynamic analysis, the

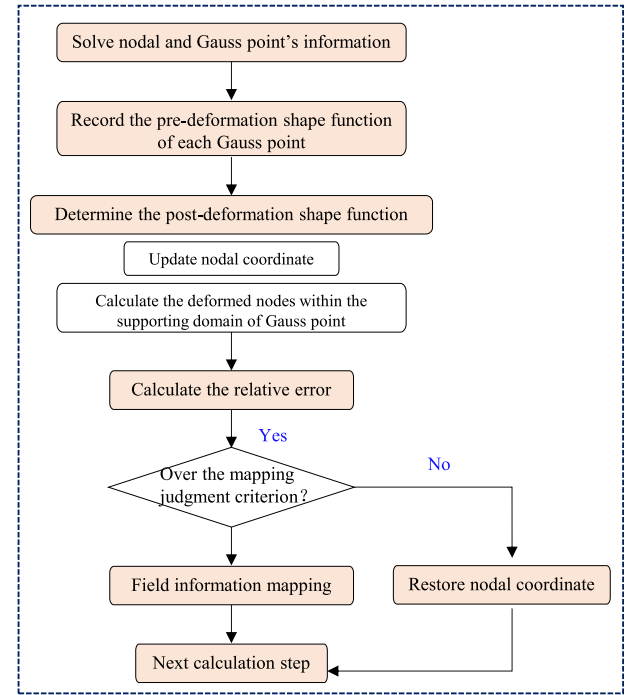


Fig. 5. Implementation of automatic time-step mapping.

time-step in Equations (39) and (40) was relatively small. For large-scale geotechnical engineering, 0.01 s has typically been used. Therefore, 2000 steps were required for the dynamic analysis of a 20 s seismic load. If RBF-based field variable mapping in the proposed method was performed in each computational step, the computational burden would significantly increase, and the accumulation of mapping errors would increase the number of unbalanced force iterations. Thus, in this study, we presented the mapping judgment criterion based on the relative error of shape function, which realized the mapping of field variable information in the time-step of a larger dynamic response, and we did not carry out mapping in the time-step of a smaller dynamic response. The relevant formula is shown in Equation (41), which established a liquefaction-induced large deformation method with automatic step mapping and improved the computational efficiency under truncation, under the premise of guaranteeing precision, and the realization flow of the automatic step mapping is shown in Fig. 5.

$$\bar{\eta} = \frac{1}{n_{\text{gauss}}} \sum \eta_i \quad \eta_i = \frac{1}{n_i} \sum \left| \frac{\phi_{i,\text{pre}} - \phi_{i,\text{post}}}{\phi_{i,\text{pre}}} \right| \quad (41)$$

where $\bar{\eta}$ denotes the average error within the analysis domain, η_i denotes the relative error of the shape function between pre-deformation $\phi_{i,\text{pre}}$ and post-deformation $\phi_{i,\text{post}}$ at the i th fixed Gauss point, n_{gauss} , n_i are the number of fixed Gauss points within the analysis domain and the number of nodes in the supporting domain of a Gauss point, respectively.

As shown in Fig. 5, the setting of the relative error value had a direct effect on automatic time-step mapping. When the setting value was small, it could not effectively reduce the number of mapping times and iterations, and when the setting value was large, it could not reflect the influence of geometric model changes on the simulation results. Martinelli and Galavi (2021) adopted a similar automatic time step mapping strategy in the material point method and effectively reduced the computational time by approximately 50 %. Consequently, numerical examples were employed in the following sections (Section 4.1 and Section 5) to quantify the impact of the automated time step mapping strategy on the accuracy and efficacy of the simulation, and we proposed a suggested value of mapping criterion.

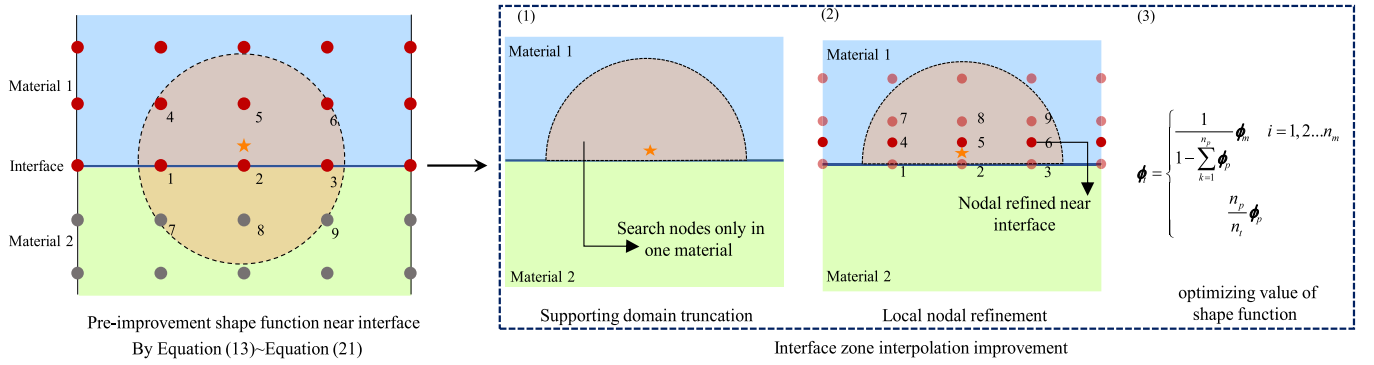


Fig. 6. Schematic showing the improved shape function near the interface between two materials.

2.3. Interface zone interpolation improvement

Localized characteristics and behavior in the interface zone between two materials will substantially differ from those within one material. Thus, if the shape function near the interface was still calculated in accordance with Equations (14) – (22), the localized characteristics and behavior would not be accurately reflected. To more effectively capture the mechanical behavior of the near-interface soil during the liquefaction-induced large deformation analysis, the domain truncation optimization and local nodal refinement algorithm were constructed to improve the calculation of the shape function. (1) The supporting domain of Gauss points at the near-interface zone only searched the nodes within one material zone, to reduce the influence of the nodes in another material when calculating the shape function. (2) We also appropriately increased the number of nodes in the zone near the interface to achieve local nodal refinement and to more accurately reflect the local stress gradient. (3) Based on the above algorithms, the value of shape function was then optimized according to the number of nodes within the supporting domain using the following equation:

$$\phi_t = \begin{cases} \frac{1}{1 - \sum_{k=1}^{n_p} \phi_p} \phi_m & i = 1, 2, \dots, n_m \\ \frac{n_p}{n_t} \phi_p & \end{cases} \quad (42)$$

where ϕ_t denotes the shape function of a Gauss point at the nodes within its supporting domain, including ϕ_p , the shape function at the shared nodes on the interface between two materials zone, and ϕ_m , the shape function at the nodes in the same material zone with the Gauss point, and n_b , n_p , and n_m reflect the relevant number of nodes.

Fig. 6 shows the comparison of the calculated shape function (pre-improvement ϕ_{pre} vs post-improvement ϕ_{post}) near the interface zone. The values of the shape function of a selected Gauss point were summarized, as shown in Equation (43), with the number of columns in the vectors equal to the number of nodes in the supporting domain.

$$\phi_{pre} = \{-0.08 \quad 0.92 \quad -0.08 \quad -0.02 \quad 0.18 \quad -0.02 \quad -0.01 \quad 0.12 \quad -0.01\} \quad (43-1)$$

$$\phi_{post} = \{-0.01 \quad 0.14 \quad -0.01 \quad 0.02 \quad 0.87 \quad 0.02 \quad -0.04 \quad 0.05 \quad -0.04\} \quad (43-2)$$

Table 1

Comparison of the two lumped mass matrices.

(a) calculated by the row-element summation method								
Nodal number	1	2	3	4	5	6	7	8
Value of main element	-0.35	1.35	-0.35	1.35	-0.35	1.35	-0.35	1.35
(b) calculated by scaled diagonal element method								
Nodal number	1	2	3	4	5	6	7	8
Value of main element	0.14	0.86	0.14	0.86	0.14	0.86	0.14	0.86

The comparison showed that the nodes in the near-interface zone had more influence on the value of the shape function after considering the above modifications, which could more realistically reflect the characteristics and behavior of the near-interface zone, and further comparisons were verified in the subsequent numerical examples.

2.4. Lumped mass matrix calculation

The mass matrix serves as a crucial component matrix for solving the equilibrium equation (Equation (9)), with its calculation method directly affecting the accuracy of the analysis. In Equation (24), the calculated \mathbf{M} served as the coordinated mass matrix, and its matrix bandwidth was large, which was not conducive to the process of storage and inverse matrix process. Therefore, the lumped mass matrix has typically been utilized rather than the coordinated mass matrix in computational methods, such as FEM. The lumped mass matrix serves as a diagonalized matrix under the assumption that the model mass will be centrally distributed at each node, and the same concept could be applied to MFLDM. The row-element summation method was adopted to obtain the lumped mass matrix in Equation (44) with the following mechanical significance. The main element of each row was equal to the sum of all elements in the row of the coordinated mass matrix, and the value at the non-main element was equal to zero:

$$(\mathbf{M}_l)_{ij} = \begin{cases} \sum_{k=1}^{n_e} (\mathbf{M})_{ik} = \sum_{k=1}^{n_e} \int_{\Omega} \rho \mathbf{N}_i^T \mathbf{N}_k d\Omega & i \neq j \\ 0 & i = j \end{cases} \quad (44)$$

Compared to the linear shape function used in FEM, the proposed MFLDM used the RBF high-order shape function to calculate the mass matrix. Therefore, if the lumped mass matrix was calculated according to Equation (44), the lumped mass matrix at the corner nodes would have negative values, which was mechanically unreasonable and would have a significant impact on the accuracy of the dynamical calculations, and even lead to the divergence of the results. This section adopted the scaled diagonal element method based on the conservation of mass law to calculate the lumped mass matrix as follows, which avoided the negative value of the lumped mass matrix at the corner nodes

$$(\mathbf{M}_l)_{ij} = \begin{cases} a(\mathbf{M})_{ii} = a \int_{\Omega} \rho \mathbf{N}_i^T \mathbf{N}_i d\Omega & i \neq j \\ 0 & i = j \end{cases} \quad (45)$$

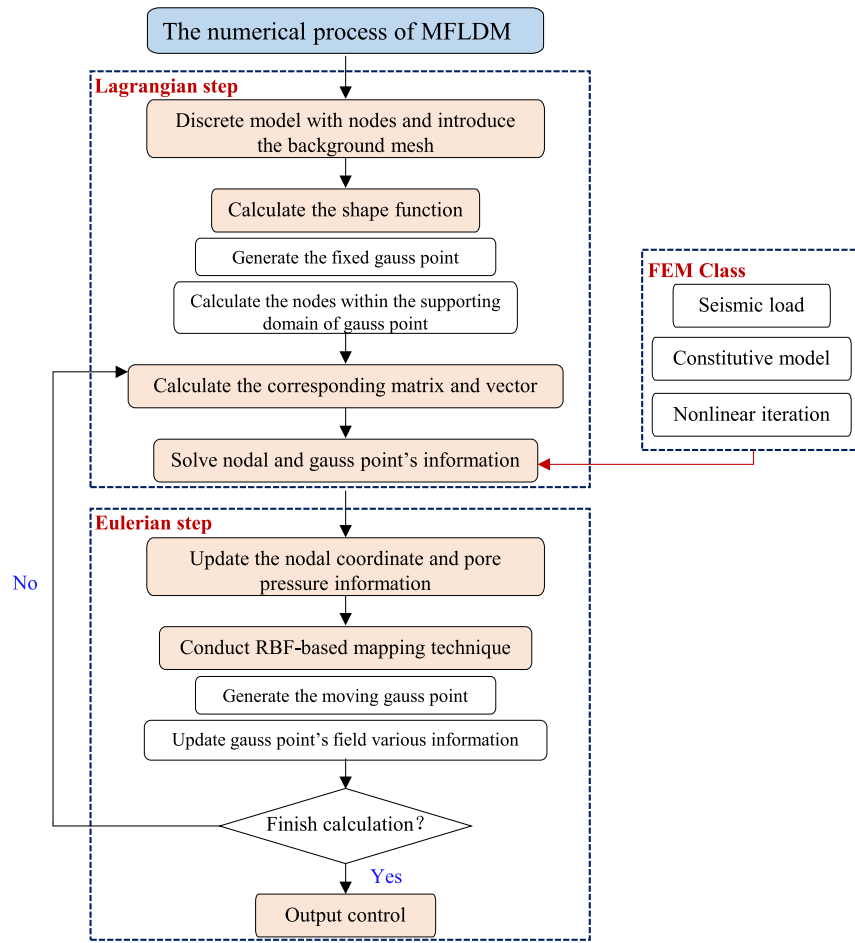


Fig. 7. Numerical implementation of MFLDM.

$$a \sum_{i=1}^{n_e} (M_{I_z})_{ii} = \rho \Omega I_d \quad (46)$$

The mechanical significance of Equation (45) was that the main element of each row in the lumped mass matrix was equal to the main element of the coordinated mass matrix multiplied by the scaling factor, whereas the value of the non-main element was zero. The value of the scaling factor was determined by the mass conservation of the model.

To compare the two lumped mass matrices, an 8-node model with the following nodal coordinates is utilized in this section: 1st node (0 m, 0 m), 2nd node (1 m, 0 m), 3rd node (2 m, 0 m), 4th node (2 m, 1 m), 5th node (2 m, 2 m), 6th node (1 m, 2 m), 7th node (0 m, 2 m), and 8th node (0 m, 1 m). Assuming the density of the material is 1 kg/m³, the size of the background mesh is 1 m × 1 m, and one Gauss point is set in each background mesh, the mass matrices computed by using Equations (44) (row-element summation method) and (45) (scaled diagonal element method) are summarized in Table 1.

By comparing the above results, we found that the lumped mass matrix calculated by using Equation (44) had a negative value at the corner node, which would have a significant impact on the accuracy of the dynamics analysis. This impact was verified in the following numerical examples, and the lumped mass matrix was calculated using Equation (45) throughout the remainder of this work.

3. Numerical implementation of MFLDM

As mentioned above, the numerical process of the proposed method was analogous to that of FEM, allowing for the full utilization of well-established FEM program codes. In this work, the MFLDM was

integrated into custom-developed FEM calculation system GEODYNA (Qu et al., 2020, Gong et al., 2021, Gong et al. (2020)), based on object-oriented and super element program technique with C++ language, which has effectively conducted static and dynamic analysis for various geotechnical projects. Consequently, the proposed method could directly invoke the constitutive models, loaders, and solvers in FEM, significantly expanding its application range and reducing its programming. Fig. 7 illustrates the numerical implementation of the proposed method.

According to the above numerical implementation, we concluded that the proposed method had the potential to couple analysis with FEM. Meanwhile, we observed that the proposed method was more complicated and time-consuming than FEM, according to the following numerical implementation processes including shape function calculation, and field variable mapping. Therefore, coupled MFLDM-FEM could address the relatively low computational load of MFLDM.

In this paper, the MFLDM was used to simulate the potential large deformation region, while FEM was used to simulate the other region (relatively small deformation). Coupled MFLDM-FEM analysis at the matrix level was also accomplished by using the shared nodes at the coupled boundaries. To ensure displacement coordination, the nodal coordinates in the FEM zone were updated after each calculation step. Subsequently, the proposed method provided an efficient technological approach for liquefaction-induced large deformation analysis in geotechnical engineering.

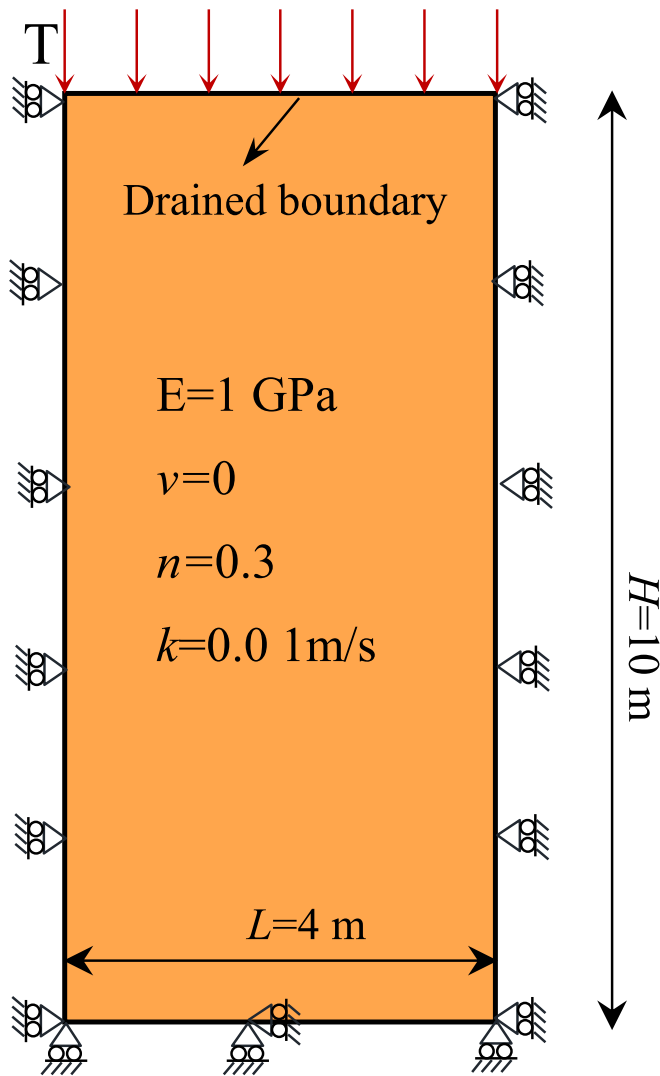


Fig. 8. Geometric model of a saturated soil column.

4. Numerical examples

4.1. Simulation of consolidation problems in a saturated soil column

Using MFLDM and the relevant program, a numerical analysis was performed to verify the accuracy and convergence of the proposed method for consolidation problems in saturated soil columns under static stresses (Yuan et al., 2019, Di and Tang, 2007). Fig. 8 shows the geometric model of the soil columns with a height of $H = 10$ m and width of $L = 4$ m. To compare the simulated results between small deformation analysis and large deformation analysis, the FEM model was established for small deformation analysis, as shown in Fig. 9 (a), with an average mesh size of $0.5 \text{ m} \times 0.5 \text{ m}$. Fig. 9 (b) shows the meshfree model with the same nodal distribution as in Fig. 9 (a), with the background mesh covering the entire model with a size of $0.5 \text{ m} \times 0.5 \text{ m}$. In addition, to study the sensitivity of the proposed method with different nodal distributions during large deformation analysis, a model with flexible nodal distribution was established, as shown in Fig. 9 (c), with the same total number of nodes and background mesh as in Fig. 9 (b). All nodes in each model were constrained horizontally, and the nodes at the bottom boundary were additionally constrained vertically. The side and bottom boundaries of the model were undrained, while the top boundary was defined as drained. In this section, the effect of automatic step mapping is discussed, and the relative error of the shape

function is first set as zero, which represents the field variable mapping process conducted in each calculation.

The solid-phase medium of the soil column was simulated using a linear elastic model with an elasticity modulus of $E = 1 \text{ GPa}$, Poisson's ratio of $\nu = 0.0$, porosity of $n = 0.3$, and permeability coefficient of $k = 0.01 \text{ m/s}$, and the liquid phase was assumed to be an incompressible medium. As shown in Fig. 10, a uniform load T was applied to the upper surface of the soil columns, and four working conditions were adopted: $T = 0.2E$, $T = 0.4E$, $T = 0.6E$, and $T = 0.8E$, with Δt set as 0.005 s . The analytical solution for a one-dimensional finite-elastic consolidation problem considering large deformation was introduced (Gibson et al., 1967). The results demonstrated that compared to conventional FEM small deformation analysis, MFLDM showed excellent agreement with Gibson's analytical solution of soil column consolidation, which validated the accuracy of the proposed method. Comparing the calculation results of models (b) and (c) revealed that MFLDM was stable and the nodal distribution had less of an impact on the calculation results.

The convergence study of MFLDM was conducted by adding four models with average nodal distances of 0.125 , 0.25 , 1 , and 2 m , based on Fig. 9 (b). Table 2 presents a summary of the normalized settlement at the upper surface of the soil column under load $T = 0.8E$, with relative deviations calculated using the 0.125 m model as the standard. The results indicated that the proposed consolidation problem had acceptable convergence.

The value of the supporting domain coefficient $alfs$, as well as shape function coefficients c and q , was subsequently investigated. First, the model in Fig. 9 (b) was adopted with load $T = 0.8E$. Subsequently, additional cases were established using $alfs$ values of 1 , 1.5 , 2 , 2.5 , ..., 4.5 , and 5 (with $c = 3$, $q = 1.03$). Compared to the analytical results for ultimate settlement at the upper surface, Fig. 11 provides a summary of the relative error for the above various cases. With the increasing value of $alfs$, more nodes were included within the supporting domain of a fixed Gauss point, and sufficient nodes were required to guarantee the simulation precision. Conversely, an excessive number of nodes could result in an increase in the dimension of the matrices related to the shape function, thereby imposing a computational burden. These findings suggested that a relative error of approximately 2% could be controlled when $alfs$ was greater than 3 ; therefore, in this manuscript, $alfs$ was equal to 3 .

Then, the study of parameters c and q was conducted. The range of value c was (with $q = 1.03$, $alfs = 3$) $[0.5, 5]$ with an interval of 0.5 , and Fig. 12 shows the relative error under different cases. When the value of c was greater than 3 , satisfactory simulation results could be obtained. In the same manner, the value of q was also examined, and the range of value q (with $c = 3$, $alfs = 3$) was $[0.5, 4.5]$, with an interval of 0.1 . According to the study of Liu and Gu (2001), the shape function may have encountered singular phenomena when q was an integer. Thus, in this examination, the adjacent value was substituted for the integer (for example, taking 0.95 , $0.96 \dots 0.9$ and 1.01 , $1.02 \dots 1.05$ rather than 1). Thus, we could conclude from the results in Fig. 13 that the relative error was minimal when q was set between $[0.96, 0.98]$ and $[1.03, 1.04]$. Consequently, $c = 3$ and $q = 1.03$ were reasonable.

Subsequently, an investigation was carried out on the impact of the automated time step mapping strategy. Using the model shown in Fig. 9 (b), six additional cases were introduced with load $T = 0.8E$. These additional cases were selected by setting the mapping criterion values to 1% , 2.5% , 5% , 7.5% , 10% , 15% , and 20% . Table 3 presents a summary of the simulation results (normalized displacement at the top surface), relative deviation, and normalized time. These findings demonstrated that the smaller judgment criteria values had a minimal impact on computing efficiency, but larger judgment criterion values led to decreased accuracy. Therefore, in a subsequent study, a judgment criterion value of 5% was suggested, which resulted in a reduction of approximately 30% in computing time while maintaining sufficient precision.

A summary of the vertical settlement at the top surface of soil

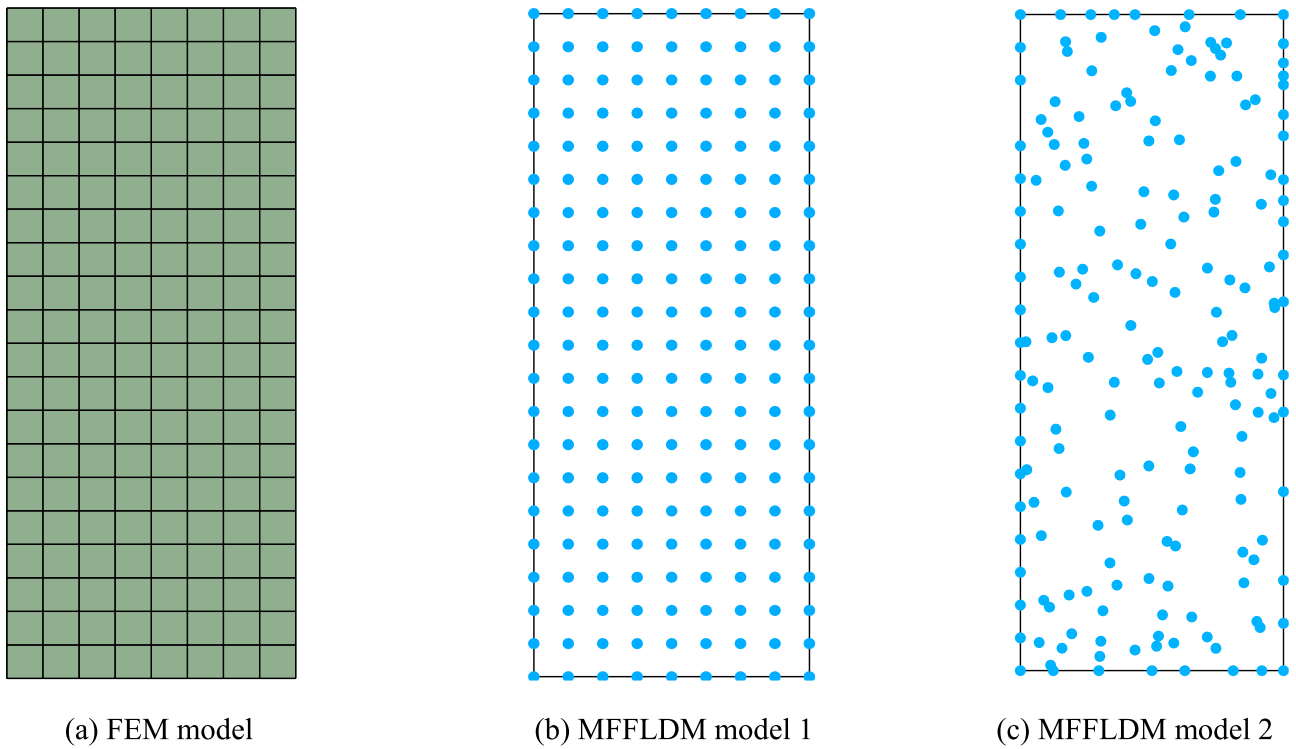


Fig. 9. Nodal/mesh model of saturated soil column.

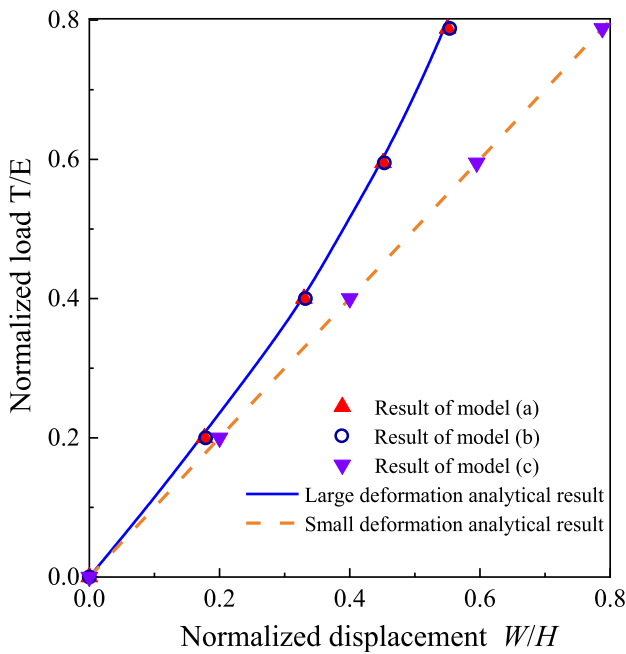
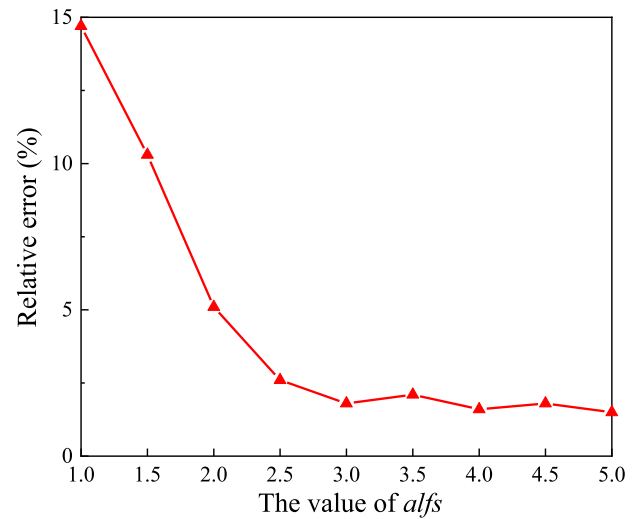


Fig. 10. Comparison of the final vertical settlement for saturated soil column.

Table 2

Convergence study of MFLD in this simulation.

	0.125 m	0.25 m	0.5 m	1 m	2 m
W/H	0.554	0.554	0.553	0.543	0.526
Relative deviations	/	0.08 %	0.17 %	2.16 %	5.05 %

Fig. 11. The relative error of final settlement at the upper surface with different $alfs$.

columns with consolidation time factor T_v is provided in Fig. 14, and the results computed using FEM small deformation analysis with model (b) are illustrated in Fig. 14 (a). Fig. 14 (b) concludes the large deformation results calculated by MFLDM analysis with model (c). For comparison, the analytical results considering the large deformation presented by Xie and Leo (2004) are also provided. The MFLDM results showed satisfactory agreement with the analytical results, which also validated the accuracy of the proposed method.

The curve trend in Fig. 15 followed a similar pattern for the above two simulations; however, in the small deformation analysis with FEM, the settlement value was obviously overestimated. We concluded that when the load was small, relative deviation between the large deformation and small deformation calculation results could be maintained

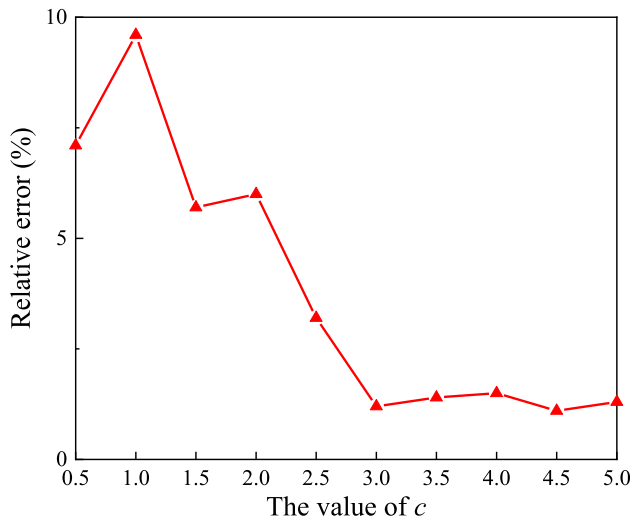


Fig. 12. The relative error with different c .

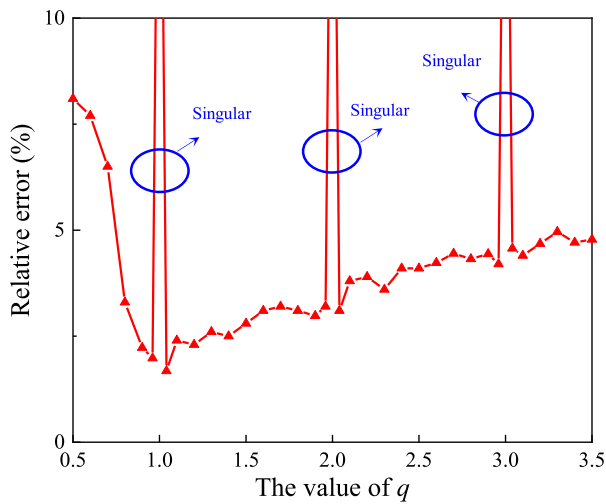


Fig. 13. The relative error with different q .

below 10 % at two typical time factors. However, as the load increased, relative deviation between the two analyses progressively increased and could reach 30 %.

4.2. Simulation of transient response problem in a saturated elastic half space

The accuracy of the proposed MFLDLM was validated in Section 4.1 with the consolidation issue, and this section presents a simulation of saturated elastic half space subjected to a uniform surface loading to discuss the precision and applicability of MFLDLM in dynamic problems. The purpose of this was to examine the accuracy and suitability of the MFLDLM in dynamic transient response issues. Fig. 16 (a) shows a sketch of the saturated elastic half space. The analytical solution of this issue under small deformation conditions was provided by Boer (1993),

Simon et al. (1984), whereas Diebels and Ehlers (1996) presented simulation results under large deformation conditions, with both results included in this section for comparison. The meshfree nodal model utilized in this section is shown in Fig. 16 (b) with a height of $H = 100$ m (decrease in the influence of boundary effect) and width of $L = 5$ m. The average nodal distance was 1 m and the size of the background mesh was $1 \text{ m} \times 1 \text{ m}$. The displacement at the bottom and the horizontal displacement of the side surface were fixed, and the pore pressure at the surface was set as zero while the side surface was set to be impermeable.

The analytical solution to this problem was provided by Boer (1993) under small deformation conditions, considering both the solid particle and fluid as incompressible materials. This section adopted the same material parameters as previous research, as shown in Table 4. The employed cyclic surface loading function was $f(t) = 3(1 - \cos 75t)$ kPa, with a time interval of 0.01 s.

Fig. 17 displays a comparison between the results obtained from the MFLDLM method and the analytical method regarding the development of pore pressure at a depth of 1 m below the surface of the half space. The well-corresponded results demonstrated the accuracy of MFLDLM in analyzing the dynamic behavior of saturated elastic porous media.

Diebels and Ehlers (1996) provided formula derivations and simulation results under large deformation conditions, with two types of applied loads: $f_1(t) = F(1 - \cos 75t)$ kPa, $f_2(t) = Fh(t)$ kPa ($h(t)$, and a Heaviside function of $h(t) = 1$ if $t \geq 0$ and $h(t) = 0$ if $t < 0$). The simulation in this section utilized the material parameters provided by Diebels and Ehlers (1996). Initially, the value of F was assigned as 3. A comparison of the top surface vertical displacement development under two different load conditions is presented in Fig. 18 and Fig. 19. The results demonstrated a high level of concurrence with the previous study under both loading conditions.

When $F = 3$, the vertical displacements on the top surface were relatively insignificant under both loading conditions. To validate the performance of MFLDLM in large deformation analysis more effectively, the amplitude F values in load $f_2(t)$ were increased to 2000, 6000, and 8000. Fig. 20 displays the relative error between small deformation and large deformation analysis. The results obtained by Diebels and Ehlers (1996) were also included for comparison. Differences between the above two results were observed at 0–1 s; however, the trends of the two results after 1 s and the final displacement were highly consistent. The comparison results once again confirmed the accuracy and capability of MFLDLM. The work conducted in this section served as an important foundation for subsequent studies in Sections 4.3 and 5.

4.3. Experimental numerical simulation of LEAP centrifuge

As shown in Section 4.1 and section 4.2, the accuracy of MFLDLM in the consolidation and dynamic problems was validated. In this section, numerical simulations of centrifuge experiments were conducted to further validate the accuracy of the proposed method in dynamic analysis for saturated soil and its applicability to the soil generalized elastoplasticity model. The Liquefaction Experiment and Analysis Projects (LEAP) was formed in 2015, consisting of Zhejiang University (ZJU), the University of Cambridge (CU), Rensselaer Polytechnic Institute (RPI), and six other research institutes. In this project, the above institutions conducted centrifuge modeling experiments on a sand slope foundation with identical specifications to provide high-quality experimental data for numerical analysis related to liquefaction (Manzari et al., 2018).

The slope foundation was 20 m wide, the slope angle was 5 m, and

Table 3

Comparison analysis with different judgment criterion values in automatic time-step mapping.

	0 %	1 %	2.5 %	5 %	7.5 %	10 %	15 %	20 %
W/H	0.553	0.554	0.557	0.557	0.559	0.562	0.579	0.591
Relative deviation	/	0.18 %	0.54 %	0.55 %	1.08 %	1.63 %	4.70 %	7.25 %
Normalized time	1 (6.2 h)	0.92	0.83	0.72	0.69	0.67	0.64	0.62

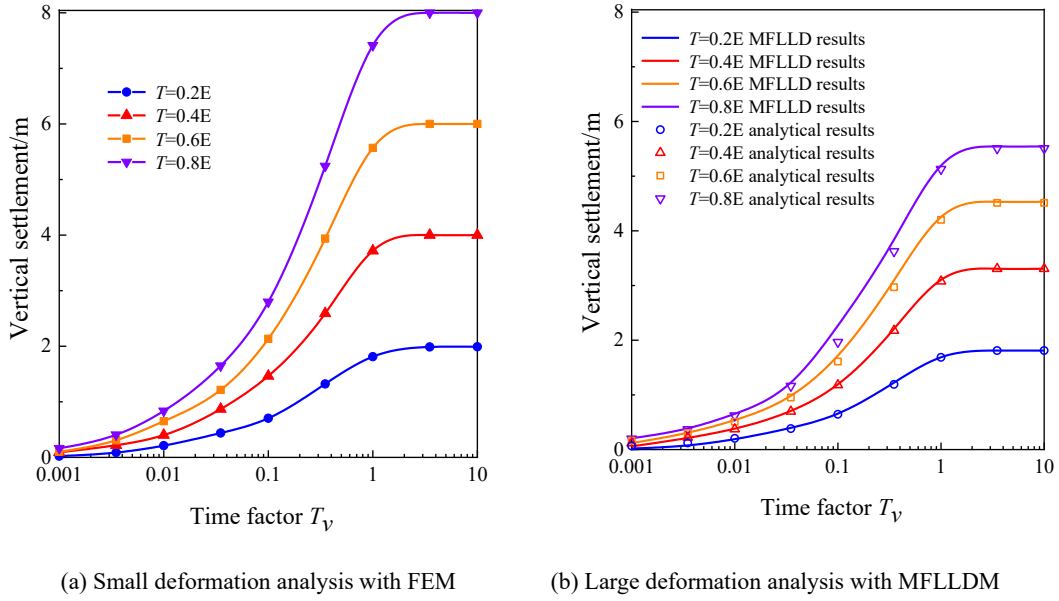


Fig. 14. Curve of vertical settlement vs. consolidation time factor.

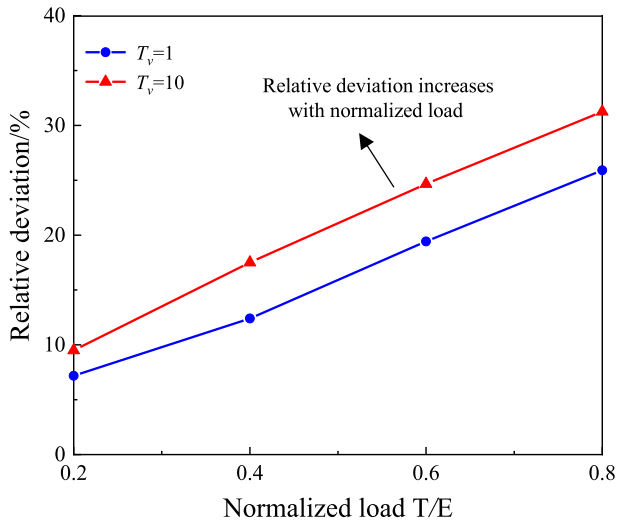


Fig. 15. Relative deviation between small deformation and large deformation analyses in this simulation.

the diameters of the two sides, as well as the middle of the foundation, were 4.875 m, 3.125 m, and 4.0 m, respectively. In this section, we selected the arrangement of displacement, pore pressure, and acceleration sensors of the RPI centrifuge (Fig. 21). The corresponding experimental results (Kokkali, et al., 2018) served as a reference for comparing the subsequent numerical simulations. As shown in Fig. 22, a model with MFLDM nodes was established, and the average displacement of the nodes was set to 0.4 m, while the background mesh size was set to 0.25 m.

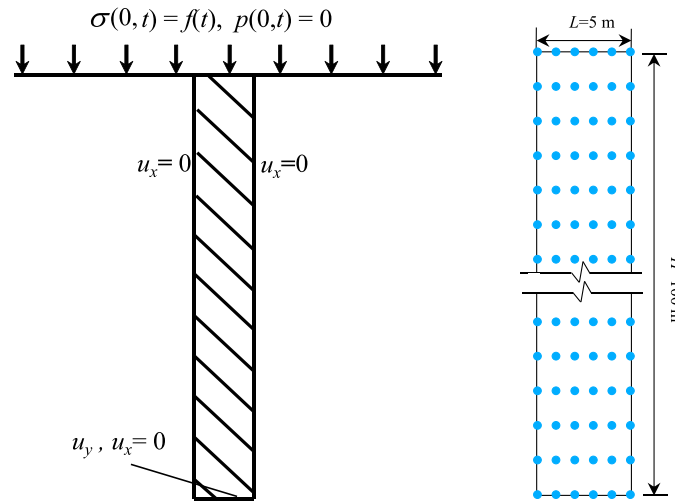
In the LEAP test, the Ottawa F-65 sand was utilized, and Vasko (2015) conducted a detailed test on this material. In this section, the generalized elasto-plastic soil model was used to simulate the characteristics of Ottawa sand. The relevant material parameters are shown in Table 5 with a pore ratio of $e = 0.572$, and the dry density of the sand was $1,652 \text{ kg/m}^3$. The horizontal and vertical permeability coefficients were taken as $k = 1.2 \times 10^{-4} \text{ m/s}$, and the frequency independent damping ratio of the soil was set as a value of 2 %, the generalized elasto-plastic theory is briefly presented in Appendix A. Dynamic calculations

were performed with a sinusoidal wave of variable amplitude (Motion 2), as depicted by the acceleration time curve in Fig. 23. The peak acceleration was 0.15 g, the time duration was 20 s, and the integration step was 0.01 s. For a more accurate simulation of the development and dissipation of pore water pressure after adynamic load, the calculation time in this section ranged from 0 to 90 s (total of 9000 steps), and the value of judgment criterion was set to 5 %.

In this simulation, static analysis was conducted under gravity, and the calculated results served as the initial stress for the dynamic analysis. Fig. 24 shows the comparison between the simulation results with MFLDM at the locations of acceleration sensors AH1–AH4 and experimental acceleration (0 – 20 s) in RPI. The results indicated that the dynamic response trend at the top and bottom of the slope foundation was consistent with the experimental results (Kokkali, et al., 2018); however, the simulation results for the top surface deviated from experimental acceleration after 10 s when compared to the bottom surface. Fig. 25 shows a comparison of the simulation results with MFLDM at the pore pressure sensors P1–P4 and the experimental excess pore water pressure (0–90 s) in RPI. Both results demonstrated the cyclic cumulative increase in EPWP with increasing dynamic load and its progressive dissipation after dynamic load. At the bottom of foundation P1, water pressure transferred to the top drainage boundary immediately after dynamic load, and we observed that it immediately dissipated after 20 s. By contrast, at the top of foundation P4, EPWP dissipated more slowly due to the above transfer from the bottom soil.

Fig. 26 shows the comparison between the simulated and experimental permanent deformation induced by dynamic load at point D1, where the simulated result of 12.2 cm was close to the experimental result of 13.6 cm. The figure also shows the simulation results using Equation (44) (with the row-element summation method). Due to the adoption of a high-order shape function in MFLDM, as noted in Section 2.2, the lumped mass matrix calculated by Equation (45) possibly contained negative values at the corner nodes, which severely impacted the stability of the calculation. As shown in Fig. 26, the dynamic results diverged at approximately 5 s, proving the necessity of modifying the calculation of the lumped mass matrix using Equation (45).

The EPWP of the slope foundation after dynamic load (20 s) is depicted in Fig. 27. As the soil depth increased, the pore pressure progressively increased, with the maximum value exceeding 30 kPa at the base of the foundation. Fig. 28 shows the nodal deformation at 20 s. In the horizontal direction, the foundation deformed to the right (the



(a) Sketch of transient response problem (b) MFLDMD nodal model utilized in this simulation.

Fig. 16. Sketch and nodal discretization of the transient response problem in a saturated elastic half space.

Table 4

Material parameters of the linear elasticity model for the saturated elastic half space.

E/MPa	ν	n	$\rho_s/(\text{Kg}/\text{m}^3)$	$\rho_f/(\text{Kg}/\text{m}^3)$	$k/(\text{m}/\text{s})$
30	0.2	0.333	2000	1000	0.01

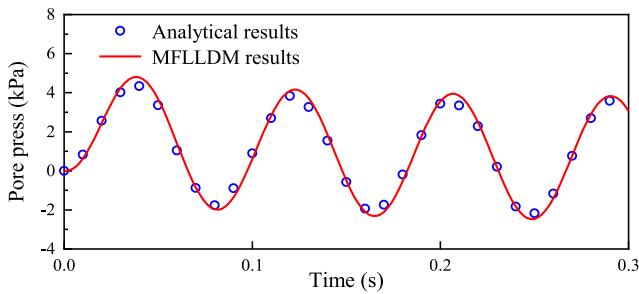


Fig. 17. Comparison of the pore pressure located 1 m below the surface of the elastic half space.

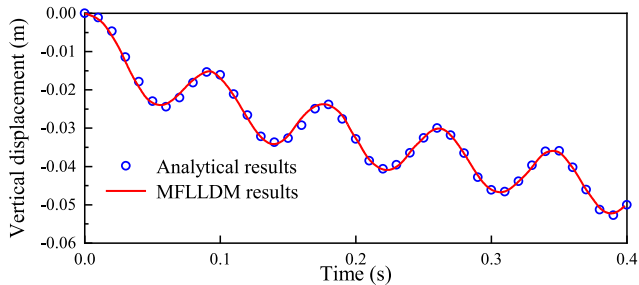


Fig. 18. Comparison of surface vertical displacement with $f_1(t)$ ($F = 3$).

maximum value was 12.2 cm). In the vertical direction, the left side of the foundation descended with a maximum value of 13.8 cm, and the right side was elevated with a maximum value of 7.5 cm. The calculation results were consistent with the deformation pattern and distribution of EPWP determined by Ghofrani and Arduino (2018) and Reyes et al. (2021).

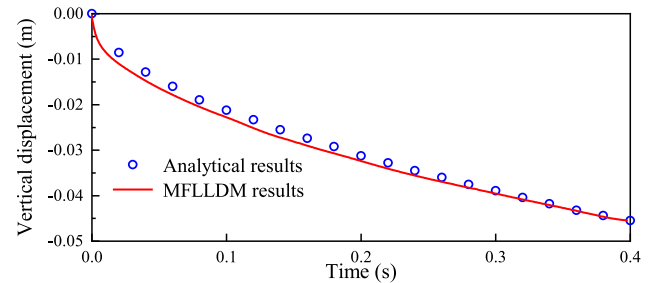


Fig. 19. Comparison of surface vertical displacement with $f_2(t)$ ($F = 3$).

Subsequently, we validated the accuracy of the proposed MFLDMD in dynamic analysis, and its applicability to the soil generalized elasto-plasticity model, providing effective technical analysis for the numerical simulation of liquefaction deformation and its safety evaluation.

5. Application of liquefaction-induced large deformation analysis for San Fernando dam

In this section, the proposed method was applied to the simulation of liquefaction damage on the San Fernando dam, reproducing the phenomenon of significant liquefaction-induced deformation on the upstream slopes under the action of a strong seismic load. In the 1971 San Fernando earthquake, the lower San Fernando earth dam sustained severe liquefaction damage, which has been extensively studied by numerous researchers (Hosseinejad et al., 2019, Wu et al., 2021, Huang and Xiong, 2017, Shantaram et al., 1976). Seed et al. (1975) noted that a significant quantity of soil liquefaction occurred in the zone between the dam body and the foundation. Consequently, the resistance of the soil was insufficient to sustain the driving force, causing upstream landslides. Actual earthquake damage indicated that the vertical settlement of the dam body and the horizontal displacement of the upstream slope were close to 20 m (Fig. 29), presenting a typical liquefaction-induced large deformation issue. Subsequently, MFLDMD was used to reproduce the damage phenomenon and locate the distribution of high pore pressure ratio regions in the dam body.

The height of the lower San Fernando dam was 44 m, and the width of the crest was 6.1 m. The geometric model and material distribution are shown in Fig. 30. As indicated in the diagram, the downstream

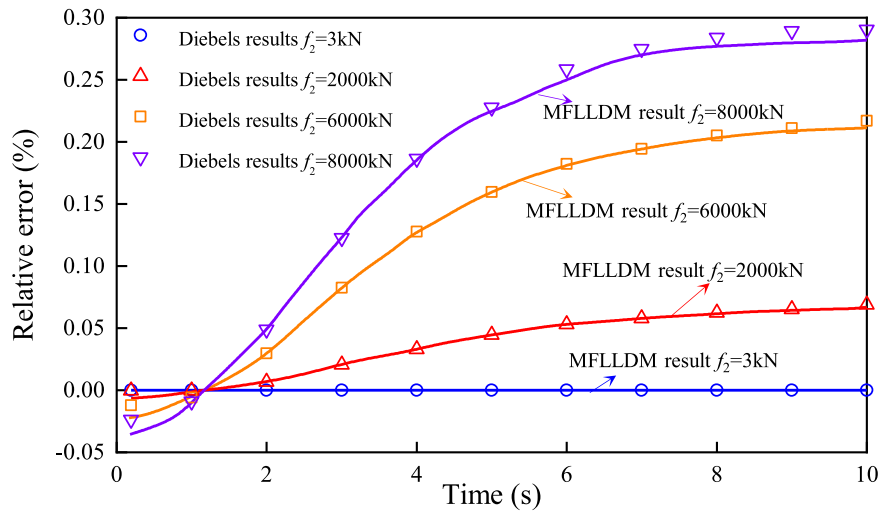


Fig. 20. Comparison of relative error with $f_2(t)$ ($F = 3, 2000, 6000$ and 8000).

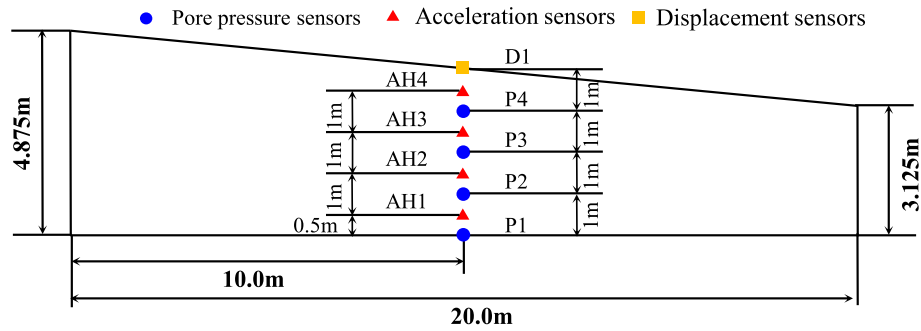


Fig. 21. Geometric model and sensor arrangement of the slope foundation.

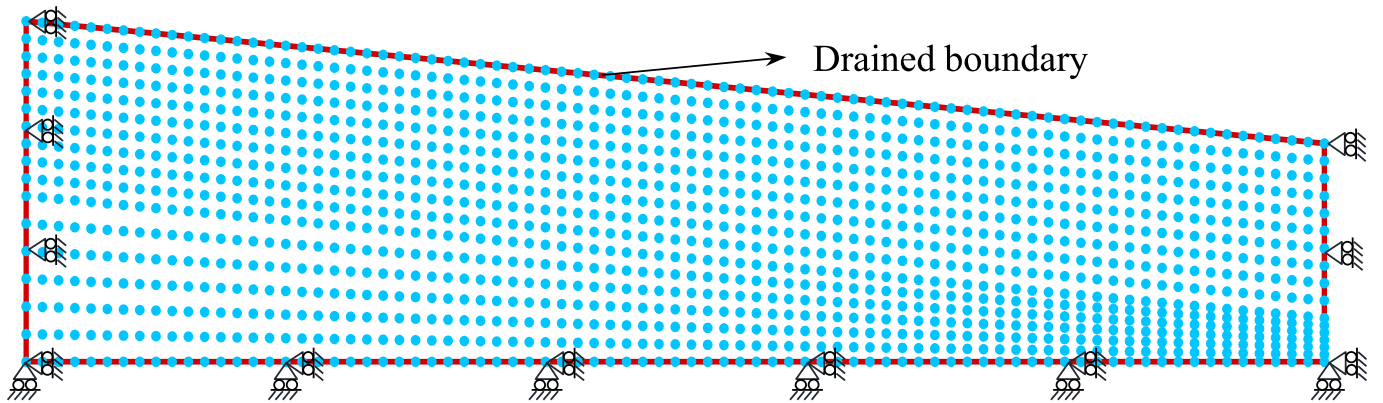


Fig. 22. Nodal distribution of the slope foundation.

Table 5

Material parameters of the generalized plasticity model for the slope foundation.

Elastic modulus				Plastic loading direction				Plastic modulus								
G_0	K_0	m_s	m_v	M_g	M_f	α_f	α_g	m_l	m_u	r_d	γ_{DM}	γ_u	β_0	β_1	H_0	H_{U0}
480	600	0.68	0.68	1.18	0.45	0.25	0.40	0.40	0.50	5	10	5	25	0.01	900	900

weight zone was placed to reinforce the dam, and when the earthquake occurred, the water level upstream of the dam was 338.1 m (33.1 m from the dam's foundation). According to previous studies (Seed et al., 1975, Ming and Li, 2003), the phreatic line inside the dam body was also

present in Fig. 30, and the zone below the phreatic line was considered saturated soil throughout this analysis. The bottom and two sides of the dam's foundation were set as undrained boundaries, while the remaining boundaries and phreatic line were considered drained boundaries.

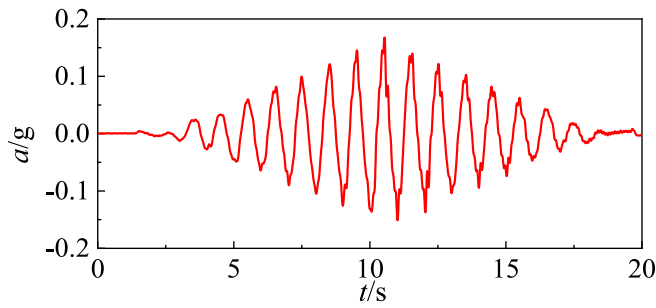


Fig. 23. Ground motion inputs in the centrifuge test.

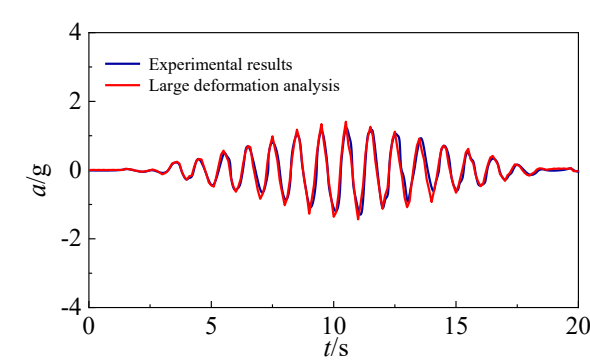
According to actual earthquake damage, the dam foundation and downstream weight zone experienced almost no deformation, so these regions were simulated with FEM mesh (node coordinates updated after each calculation step). The remaining material partition was discretized using meshfree nodes, where the average nodal displacement was controlled to be 0.5 m. A model with global discretization using mesh-free nodes was also added for comparative analysis. The refined nodal distribution was performed at the interface between the dam body and the foundation, and the improvement in shape function in Section 2.3 was also implemented to capture the local soil characteristics in both models.

The properties of the dam construction materials were investigated using standard penetration and triaxial tests. Because the upstream slope of the dam was damaged and reconstructed, information could not be obtained. However, it is generally believed that the upstream and downstream soil properties were similar. Several scholars have extensively researched the soil parameters (Seed, 1973; Seed et al., 1975), Ming and Li (2003) for the San Fernando Dam. Among these studies,

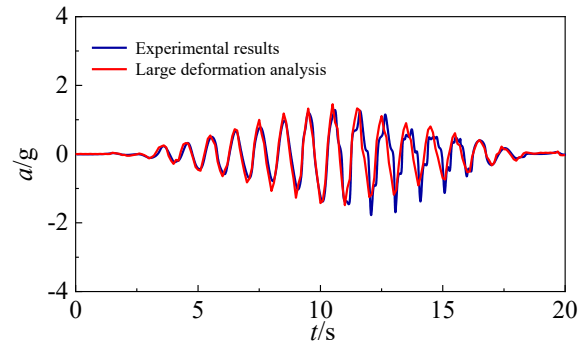
Ming and Li (2003) specifically focused on the elasto-plastic parameters of the dam body, thus, the parameter selection in this section primarily relied on these suggested values. According to Fig. 30, the dam body could be divided into the rolled fill zone, hydraulic fill zone, alluvium zone, and clay zone. All above zones in the dam were described by the generalized elasto-plastic model using the same material parameters (Table 6), with initial void ratios of 0.660, 0.500, and 0.567 assigned to the hydraulic fill zone, rolled fill zone, and alluvium zone, respectively. A field investigation between 1985 and 1987 found that the soil in the clay core was a mixture of silty clay and sandy soils. Due to a lack of detailed information on the soils in the clay zone, in this analysis, the clay zone was simplified and treated as a hydraulic fill with lower permeability. The coefficients of permeability assigned to the subregions were as follows: horizontal permeability coefficient $k_h = 1 \times 10^{-5}$ m/s and vertical permeability coefficient $k_v = 4 \times 10^{-6}$ m/s for the alluvium zone, $k_h = 1 \times 10^{-4}$ m/s and $k_v = 4 \times 10^{-5}$ m/s for the hydraulic fill zone, and $k_h = 5 \times 10^{-6}$ m/s and $k_v = 2 \times 10^{-6}$ m/s for the clay and the rolled fill zone, respectively.

Based on the above material parameters, a verification study was conducted. Fig. 31 illustrates the simulated stress path (shear stress – effective mean principal stress) for the hydraulic fill zone soil under undrained cyclic simple shear conditions. The initial confining pressure was isotropic with a value of 100 kPa and a cyclic stress ratio of $\tau/p'_0 = 0.15$. The cyclic stress ratio-failure vibration results are summarized in Fig. 32. The simulated results demonstrated good concurrence with previous research conducted by Seed, 1973 and Moriwaki et al. (1988), which verified the feasibility of the generalized elasto-plastic model and corresponding material parameters in this section.

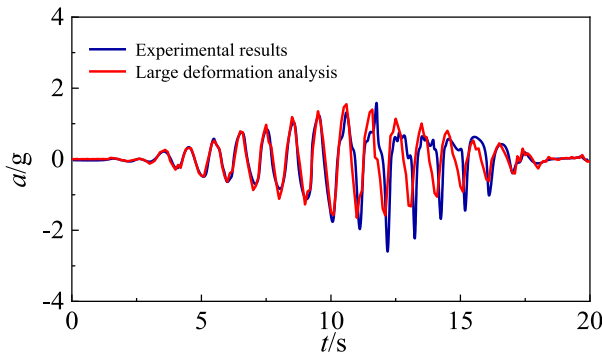
The bottom and two sides of the dam's foundation were set as undrained boundaries, while the remaining boundaries were considered drained boundaries. The initial dynamic stress was calculated through static analysis under self-weight. Fig. 33 shows the Pacoima acceleration



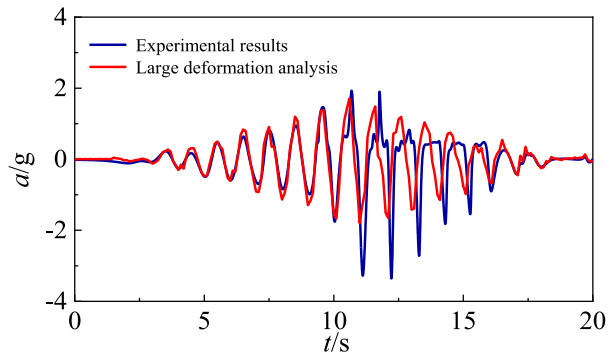
(a) AH4



(b) AH3



(c) AH2



(d) AH1

Fig. 24. Comparison of the simulated and experimental results for acceleration.

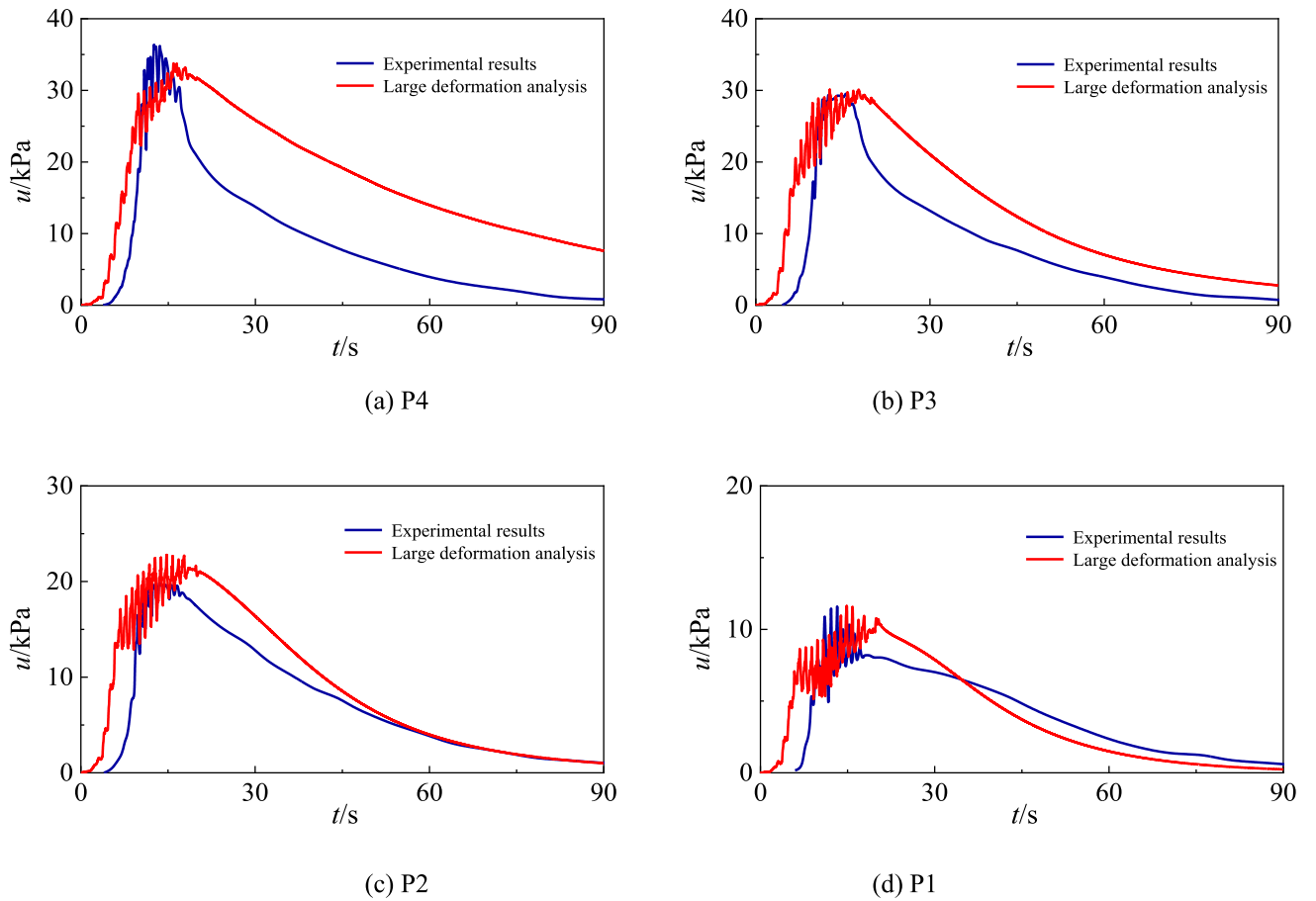


Fig. 25. Comparison of the simulated and experimental results for excess pore water pressure.

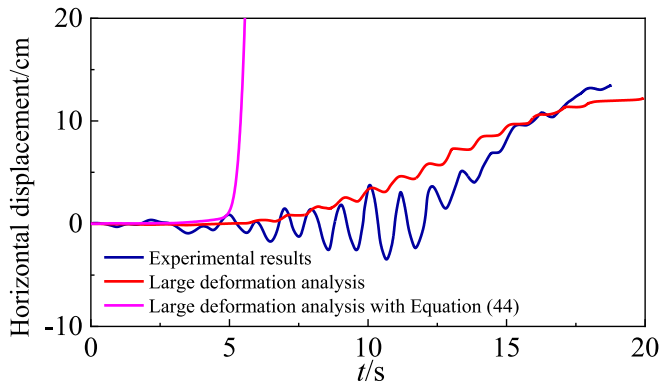


Fig. 26. Comparison of the simulated and experimental results for horizontal displacement.

curve (CSMIP 1999) for dynamic analysis with a peak acceleration of 0.6 g. Input ground motion was achieved using a viscoelastic boundary and an equivalent load, and relevant information can be found in [Appendix B](#). In this simulation, the duration for dynamic analysis was 30 s, and the integration interval was 0.005, with the judgment criterion value set to 5 %.

Fig. 34 depicts the nodal deformation of the dam at typical times (0 s, 8 s, 15 s, 20 s, and 30 s). The results indicated that the dam did not deform significantly during the early stage of the earthquake. However, as seismic load increased, excess pore water pressure progressively accumulated. Vertical settlement of the dam body occurred, with a maximum value of 15.9 m at the top of the dam. Subsequently, the dam slope experienced sliding deformation pointing upstream, with the largest value of 17.9 m. With relatively small horizontal and vertical displacements of the downstream weight zone, deformation of the downstream slope was prevented. Consequently, the downstream slope of the dam did not experience liquefaction-induced large deformation compared to the upstream slope. The results of this simulation were consistent with previous studies ([Ming and Li, 2003](#), [Huang and Xiong, 2017](#), [Hosseinejad et al., 2019](#), [Talbot et al., 2024](#)), confirming the

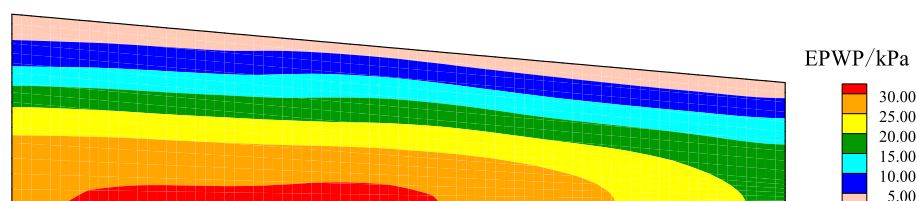


Fig. 27. Distribution of excess pore water pressure at 20 s.

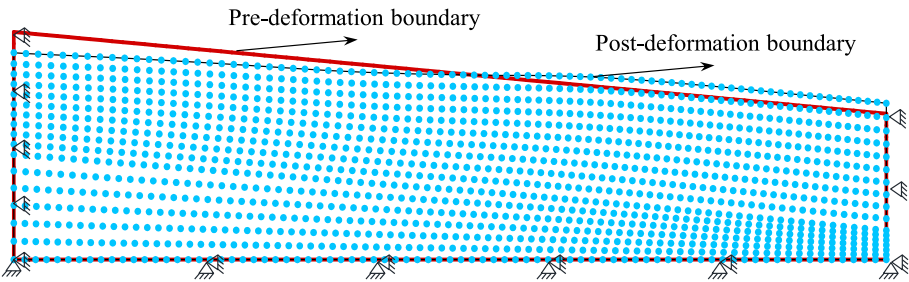


Fig. 28. Nodal deformation of the slope foundation at 20 s (magnification: 5 ×).

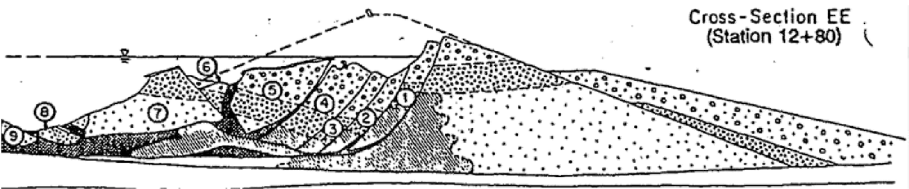


Fig. 29. Seismic failure phenomenon of the lower San Fernando dam.

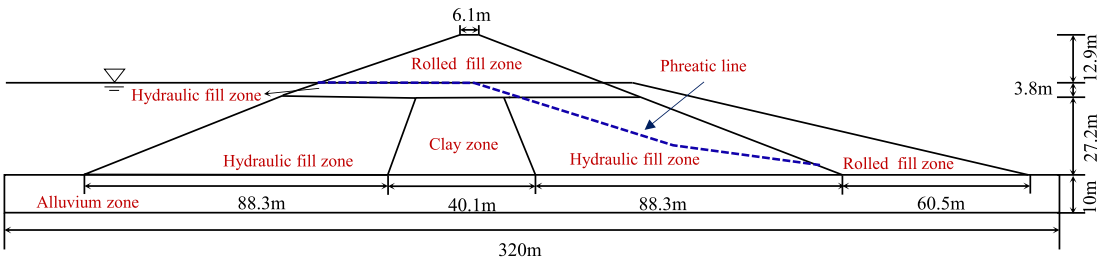


Fig. 30. Geometric model and material partitions of the lower San Fernando dam.

Table 6
The material parameters of the generalized plasticity model for the San Fernando Dam.

Elastic modulus				Plastic loading direction				Plastic modulus								
G_0	K_0	m_s	m_v	M_g	M_f	α_f	α_g	m_l	m_u	r_d	γ_{DM}	γ_u	β_0	β_1	H_0	H_{U0}
125	210	0.47	0.47	1.38	1.02	0.30	0.30	0.50	0.50	5	10	5	25	0.01	600	600

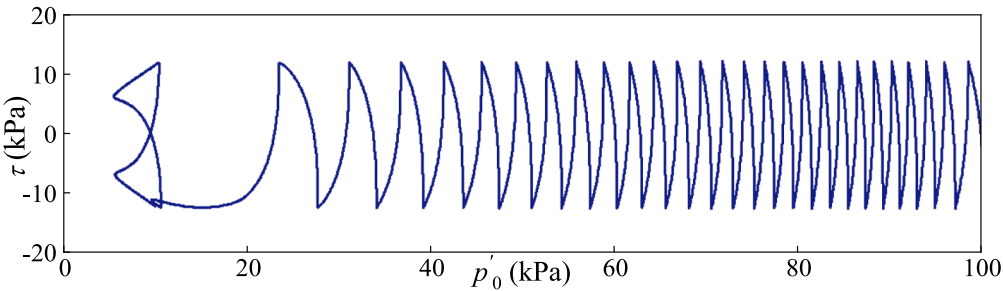


Fig. 31. Simulated stress path (shear stress – effective mean principal stress) for hydraulic fill zone soil.

applicability of the proposed MFLDM for addressing the liquefaction-included large deformation problem. In addition, due to the limitations of the soil constitutive model, the MFLDM and previous simulation methods (i.e., FEM and MPM) could not fully reproduce the actual observed phenomenon where the upstream slope of the San Fernando Dam failed a few minutes after the earthquake.

Table 7 shows the comparison of the coupled model (MFLDM-FEM)

and global MFLDM model results, including maximum horizontal displacement, maximum vertical displacement, and normalized analysis times. Due to the small deformation of the dam foundation and downstream weight zone, the results of the two calculations were nearly identical, validating the feasibility of coupled analysis. Meanwhile, using FEM in small deformation zones allowed the coupled analysis to circumvent the relative computational inefficiency of MFLDM.

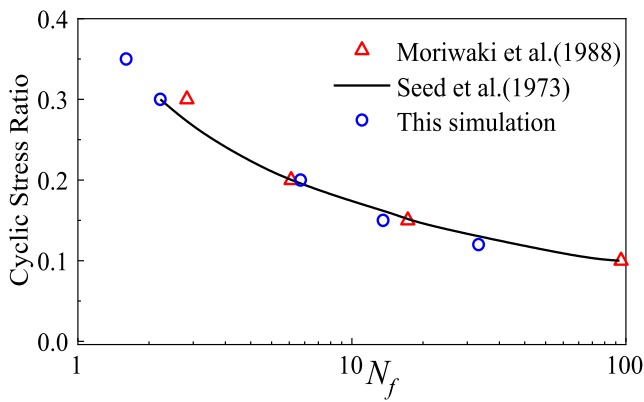


Fig. 32. Comparison of cyclic stress ratio – failure vibration curve.

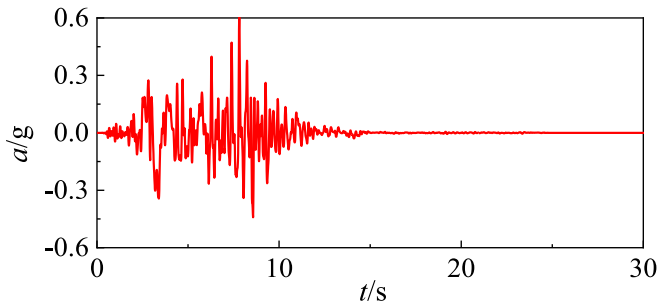


Fig. 33. Acceleration time history curve for San Fernando dam dynamic analysis.

The 5 % judgment criterion value was established based on the discussion in Section 4.1. Subsequently, a comparative analysis was carried out, considering both cases with and without automatic time-step mapping. The mapping times conducted every 0.5 s during analysis for 0–30 s is illustrated in Fig. 35, where the maximum value was 100 in 0.5 s. According to the results, the seismic wave acceleration was relatively small between 0 and 5 s, and the dam body almost did not deform. As a result, automatic time-step mapping was also small. After 5 s, the dam body experienced obvious deformation in both the horizontal and vertical directions as seismic wave acceleration increased, accompanied by a progressive increase in the mapping process times. The earthquake was over after nearly 15 s; however, dam deformation persisted, so the times required for automatic mapping remained large. Table 8 provides a summary of the total times of mapping and computational time for the two cases. Based on the results, we concluded that the total mapping time was 3268 throughout the analysis after the implementation of automatic time-step mapping techniques, which was a 46 % reduction compared to the case without these techniques. Because the two cases in the Lagrangian step were almost the same, the total computational time was reduced by 26 % after considering the automatic time-step mapping techniques.

In this simulation, the frequency independent damping ratio of the soil was set as a value of 2 %. To further confirm the reasonableness of employing Rayleigh damping, research was conducted to study the impact of various damping ratio values (0.1 %, 1 %, 2 %, 5 %, 7.5 %, and 10 %) on the precision. Table 9 shows that when the damping ratio values were less than 5 %, the simulation results, including the maximum horizontal displacement and maximum vertical displacement, were almost identical. Thus, Rayleigh damping and its values utilized in this manuscript were acceptable.

Fig. 36 shows the nodal displacement time history curve at the maximum vertical displacement point A (top of the dam body) and the maximum horizontal displacement point B (near the upstream slope).

The results indicated that the body of the dam continued to deform throughout the dynamic analysis duration. During the period from 5 to 10 s, nodal displacement rapidly accumulated due to large acceleration, and displacement accumulation progressively slowed down as the seismic load decreased. At 15 s, however, the vertical velocity at point A and the horizontal velocity at point B were 0.47 and 0.94 m/s, respectively, indicating that deformation of the dam continued after the earthquake, which was consistent with the actual earthquake damage.

To examine the effects of the mapping error-induced non-consistency condition at the Gauss point on simulation precision, this section presented a comparative analysis of the shear stress time history curve of a Gauss point subjected to seismic load (type 1, which involved utilizing the mapping function in Equation (36) vs. type 2, which involved calculating the constitutive model variables from the mapped stresses, strains, and stress histories), as illustrated in Fig. 37. The results indicated that the time history curves computed using two different types of conveying the constitutive model variables were nearly identical (with 2 % relative deviation). However, compared to type 1, type 2 numerical implementation was more difficult and time-consuming (13.5 h for type 1 and 19.3 h for type 2). Therefore, this work demonstrated that calculating constitutive model variables via the mapping function was reasonable.

Fig. 34 shows the deformation of the dam, to locate the damaged surface of the San Fernando Dam during liquefaction-induced large deformation, Fig. 38 presents the distribution of accumulated plastic strain in the San Fernando dam at 30 s. The accumulated plastic strain extended from toe of upstream dam slope to the left side of the dam crest, forming a significant shear band within this region. This shear band corresponded to the main damage surface observed in actual earthquake damage (Fig. 29), and a similar conclusion was reached by Feng et al. (2021) using MPM simulation.

The simulation verified the effect of the improved shape function proposed in Section 2.3. Compared to the dam body material, the dam foundation material had a higher modulus and showed minimal deformation during the seismic loads. Thus, the sliding deformation of the dam body was influenced if the value of the shape function at the shared nodes (in the interface boundary) made a significant contribution to the Gauss point. Fig. 39 shows the nodal deformation at 30 s without shape function improvement. The maximal horizontal and vertical displacements were 19.4 and 20.2 m, respectively. However, without considering shape function improvement, the upstream slope almost did not slide due to dam foundation constraint, which was inconsistent with the actual seismic damage. Thus, the necessity of the proposed shape-function enhancement near the interface of two materials was confirmed.

Fig. 40 illustrates the EPWP distribution of the dam body after the earthquake, where the high EPWP zone was concentrated at the bottom of the dam body and soil foundation. Compared to the previous studies by Ming and Li (2003), Menon and Song (2023), and Feng et al., (2021), the simulation results in this section were consistent in the overall distribution, although there were some differences in the maximum value of EPWP. Fig. 40 also presents the time history curve of EPWP at point C, which was located at the interface between the dam body and foundation, and had a maximal value of 342 kPa. The results indicated that EPWP built up cyclically during seismic load and stabilized 15 s after the earthquake. The process of pore pressure dissipation was not further simulated in this study due to the relatively low permeability coefficient.

Fig. 41 shows the distribution of the EPWP ratio of the dam body after the earthquake, indicating that a large zone of high pore pressure ratio areas (greater than 0.7) was present at the bottom of the dam body and near the upstream and downstream dam slope. Meanwhile, the liquefaction extent near the upstream slope was greater than that of the downstream slope. Ming and Li (2003) and Feng et al. (2021) calculated the high EPWP region in accordance with this work. In addition, Seed et al. (1975) considered the clay zone as non-liquefiable soil, resulting in the restriction of its high EPWP ratio zone only located near the

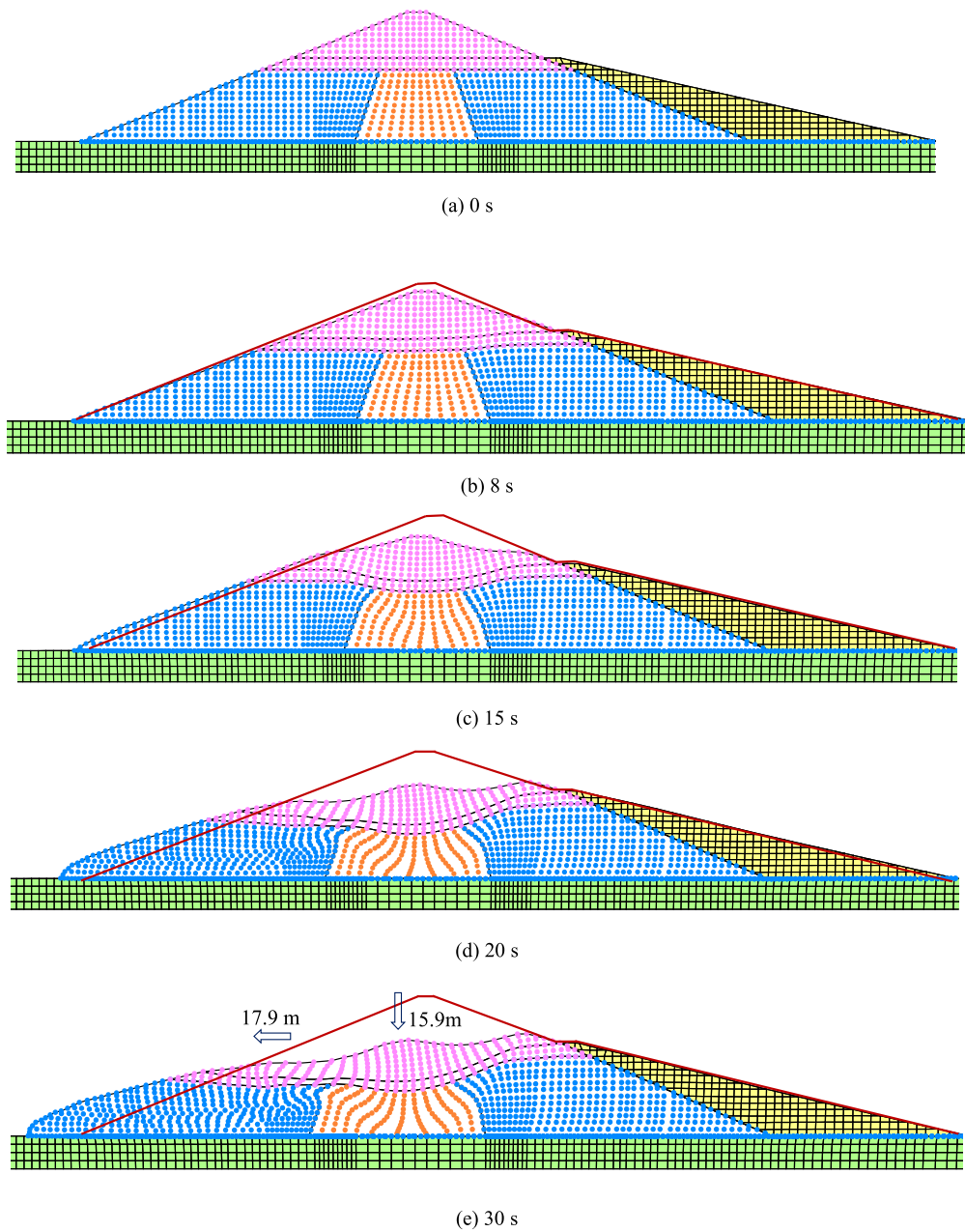


Fig. 34. Nodal deformation of the lower San Fernando dam at typical times.

Table 7
Comparison of the coupled model (MFLDM-FEM) and global MFLDM model.

	Maximum horizontal displacement	Maximum vertical displacement	Normalized analysis time	
			Static	dynamic
Coupled model	17.9 m	15.8 m	1 (0.89 h)	1 (18.2 h)
Global MFLDM model	17.9 m	15.9 m	1.19	1.64

upstream and downstream dam slopes. The high EPWP ratio zone represented a high risk of liquefaction in the above area, which reduced the effective tension in the soil body. If the resistance was insufficient to withstand the propelling force, liquefaction-induced large deformation

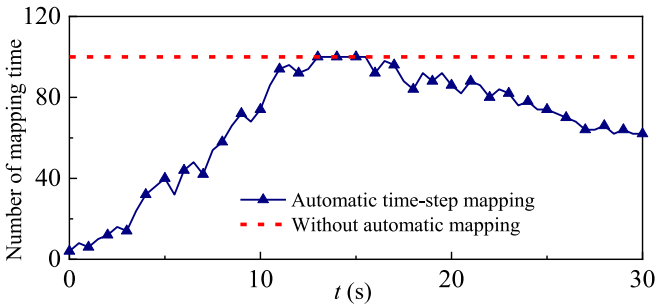


Fig. 35. Times of field variable mapping performed in every 0.5 s.

could occur. According to nodal deformation at typical times (Fig. 24) and the distribution of post-seismic pore pressure ratio (Fig. 29), the

Table 8

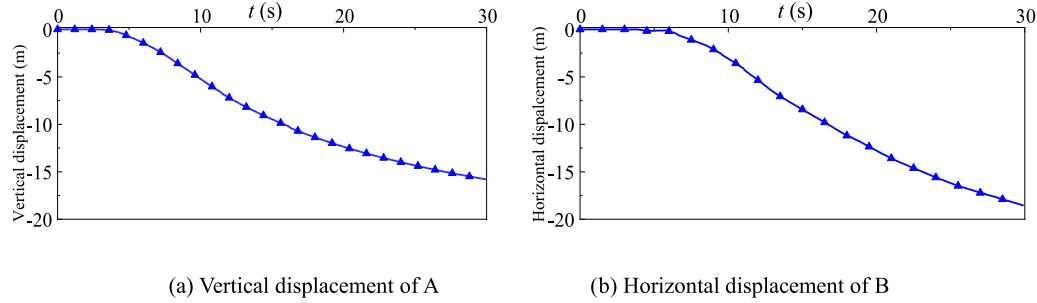
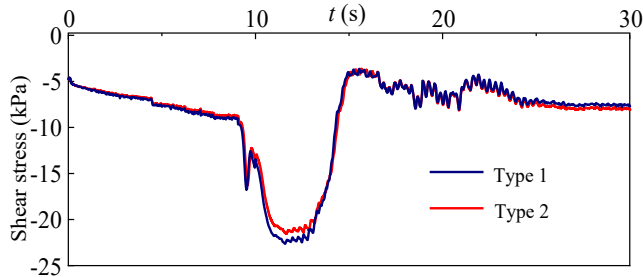
Comparison of total mapping times and normalized computational times of the two cases.

	Total mapping times	Computation time	Normalized time
With automatic mapping	3268	13.5 h	0.74
Without automatic mapping	6000	18.2 h	1

Table 9

A comparison study of various damping ratios.

Damping ratio values	0.1 %	1 %	2 %	5 %	7.5 %	10 %
Maximum horizontal displacement	15.9 m	15.9 m	15.9 m	15.8 m	15.5 m	15.2 m
Maximum vertical displacement	18.0 m	18.0 m	17.9 m	17.7 m	17.4 m	16.8 m

**Fig. 36.** Time history curve of nodal deformation.**Fig. 37.** Comparison of the shear stress of a Gauss point under seismic load (type 1 vs type 2).

downstream slope was also at risk of liquefaction-induced large deformation. However, the presence of the downstream weight zone prevented further development of deformation and guaranteed the safety of downstream slopes. To verify this hypothesis, the liquefaction-induced large deformation analysis was continued in this study without considering the downstream weight zone, and the post-seismic nodal deformation results are depicted in Fig. 42. Compared to Fig. 24, the vertical settlement of the dam body in this simulation increased to 16.2 m, while the maximum sliding deformation values of the upstream and downstream dam slopes were 8.7 m and 18.1 m, respectively.

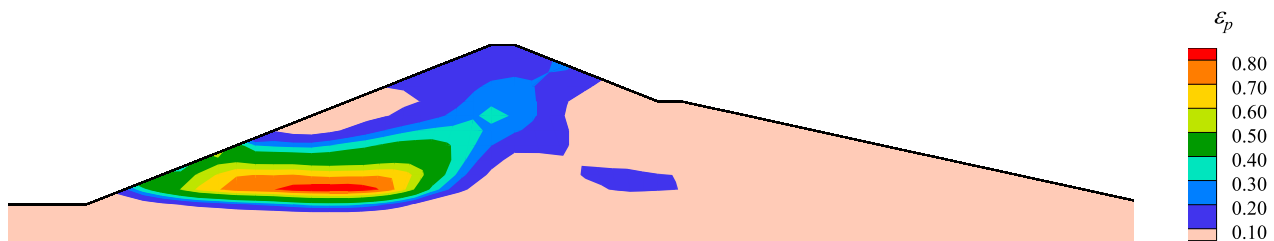
In summary, MFLDLM could more realistically and effectively reproduce the development of liquefaction damage of the San Fernando

Dam under strong seismic load. This simulation also validated the need for proposed shape function improvement near the interface of the two materials. The potential liquefaction zone was localized by the distribution of a high pore pressure ratio, which indicated that the effective tension of soil in this region was reduced and the resistance was insufficient to withstand the driving force, and as a result, sliding deformation could occur.

6. Conclusions

In this study, we presented a practical MFLDLM to achieve effective stress-excess pore water pressure analysis for saturated soil. The preliminary results and recommendations were provided through two typical numerical examples and the liquefaction damage of the San Fernando Dam under strong seismic load, as presented below.

- (1) The proposed method constructed fixed-moving Gauss points and introduced the field variable mapping technique based on RBF to realize the spatial re-distribution of the stress state and pore-pressure information during deformation, providing effective technical support for liquefaction-induced large deformation analysis.
- (2) The relative error of the shape function was suggested as the judgment criterion for automatic time-step mapping. When the value was set to 5 %, the total mapping times could be

**Fig. 38.** Distribution of accumulated plastic strain in San Fernando dam at 30 s.

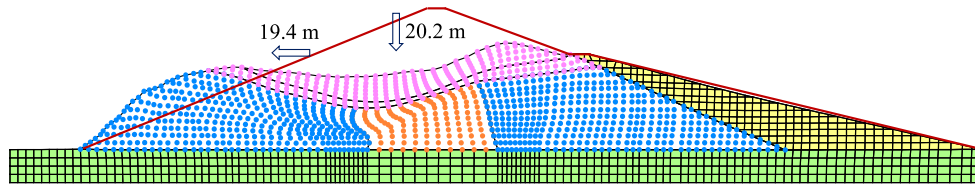


Fig. 39. Nodal deformation at 30 s without considering the shape function correction.

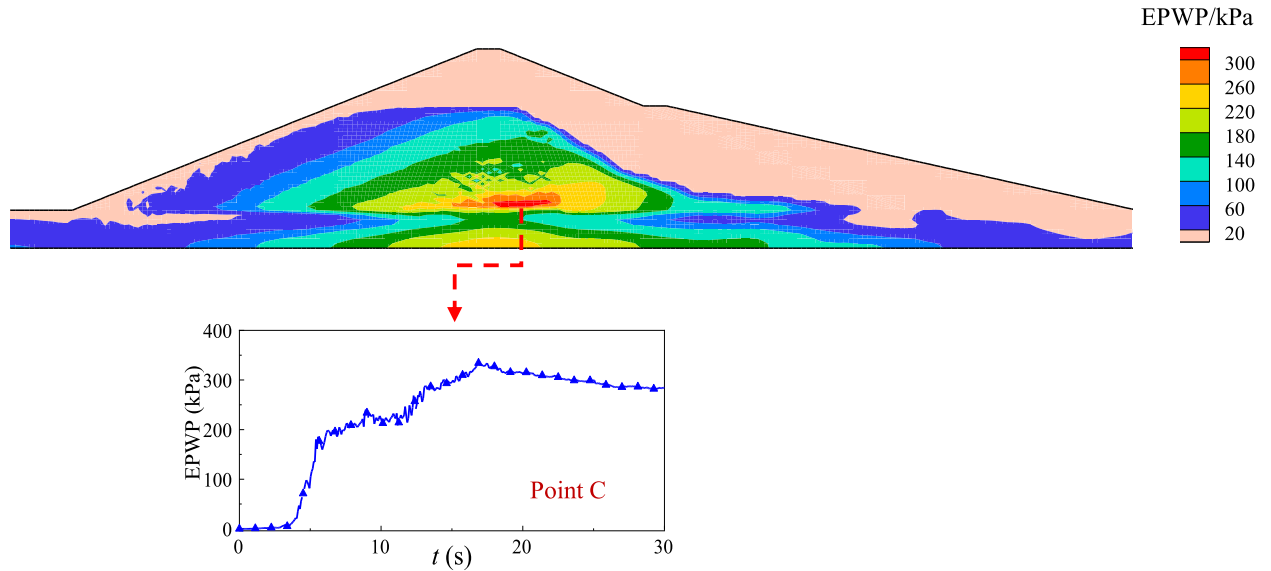


Fig. 40. Distribution of post-earthquake excess pore water pressure and nodal excess pore water pressure time history curve at point C (kPa).

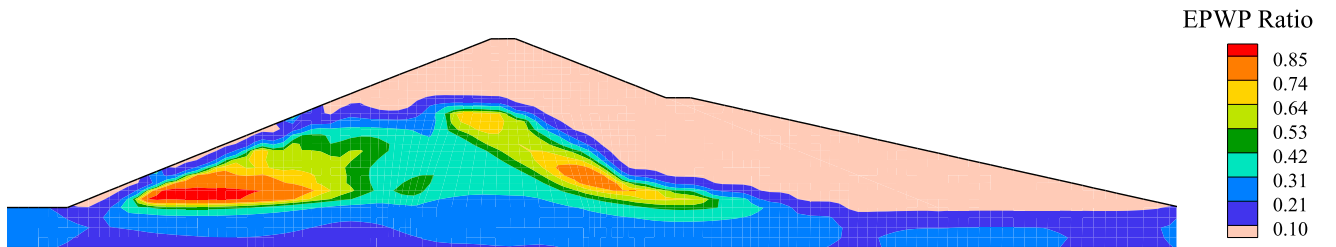


Fig. 41. Distribution of post-earthquake excess pore water pressure ratio.

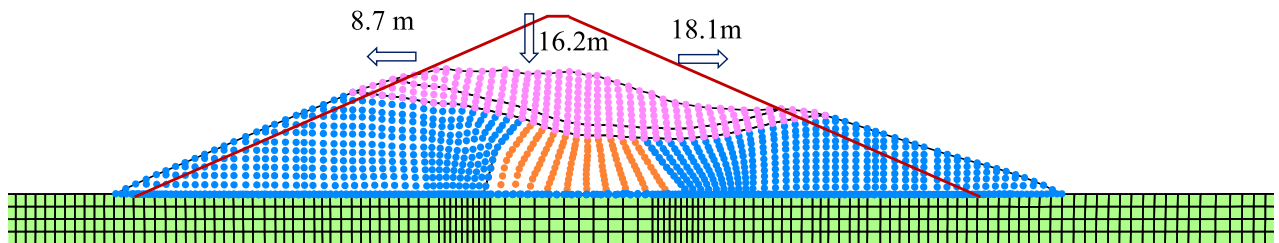


Fig. 42. Nodal deformation at 30 s without downstream weight zone.

- significantly reduced, and the computation time decreased by approximately 30 % while ensuring the accuracy of the analysis.
- (3) The improved shape function in the near-interface zone was developed by using domain truncation optimization and the local nodal refinement algorithm, which could more reasonably reflect the shear deformation characteristics of the soil body in the near-interface region.

- (4) Through comparative analysis, we found that the high-order shape function used in MFLDM could lead to negative values of the lumped mass matrix at the corner nodes calculated by the row-element summation method. Notably, the scaling diagonal element method used in this study could effectively solve the above problem.

- (5) By simulating a consolidation problem for a saturated soil column, transient response problem in a saturated elastic half space and the LEAP centrifuge experiment, the accuracy, convergence, and applicability to the soil generalized elasto-plastic model of the proposed method in consolidation and dynamic analysis were verified.
- (6) The MFLDLM was applied to the simulation of liquefaction damage of the San Fernando Dam, reproducing the liquefaction-induced large deformation phenomenon of the upstream dam slope and locating the high pore pressure ratio zone under strong seismic load. We found that the effective stress of soil in the potential liquefaction risk region was reduced, and when the resistance was not sufficient to withstand the driving force, sliding deformation could occur.

CRediT authorship contribution statement

Jin Gong: Project administration, Methodology, Formal analysis, Data curation, Conceptualization. **Degao Zou:** Software, Resources, Methodology, Funding acquisition. **Xianjing Kong:** Validation, Supervision. **Jingmao Liu:** Writing – review & editing, Writing – original draft. **Kai Chen:** Methodology. **Yongqian Qu:** Visualization, Software.

Xiang Yu: Writing – review & editing, Writing – original draft.

Declaration of competing interest

The authors declare that they have no known competing financial interests or personal relationships that could have appeared to influence the work reported in this paper.

Data availability

No data was used for the research described in the article.

Acknowledgements

The research work described in this paper was supported by the China Postdoctoral Science Foundation Funded Project (Grant No.: 2023 M730477), National Natural Science Foundation of China (Grant No. 51890915, 52192674, U23B20149). Key Research & Development and Promotion Projects-Science and Technology in Henan Province (No. 242102321112). The authors would like to greatly acknowledge all the financial support and express their sincerest gratitude.

Appendix A. Generalized elasto-plastic theory.

The generalized elasto-plastic theory was provided by Pastor et al. (1985) with the advantage of not requiring the explicit yield surface and plastic potential surface. Based on the above theory, a generalized elasto-plastic model (Liu et al., 2018, Zienkiewicz et al., 1985) for civil engineering structures was devised for the static and dynamic analysis of civil engineering structures. The model was concisely presented using the following equations formulated in p (mean stress)- q (deviatoric stress) space.

In this manuscript, the generalized elasto-plastic model was integrated into custom-developed FEM software GEODYNA as a constitutive model class. The generalized elasto-plastic model provided a constitutive matrix (relationship between stress and strain) \mathbf{D}^{ep} for MFLDLM in calculating the stiffness matrix \mathbf{K} and stress vector σ as follows:

$$\mathbf{K} = \iint_{\Omega} \mathbf{B}^T [\mathbf{D}^{\text{ep}}] \mathbf{B} d\Omega \quad (\text{A.1})$$

$$\{d\sigma\} = [\mathbf{D}^{\text{ep}}] \{d\varepsilon\} \quad (\text{A.2})$$

where \mathbf{B} is the displacement-strain matrix.

The strain can be divided into elastic strain vector and plastic strain vector, and we can multiply elastic the constitutive model \mathbf{D}^e on both sides of the equation:

$$[\mathbf{D}^e] \{d\varepsilon\} = [\mathbf{D}^e] \{d\varepsilon^e\} + [\mathbf{D}^e] \{d\varepsilon^p\} \quad (\text{A.3})$$

In the elastic phase, \mathbf{D}^e can be obtained by shear bulk moduli G and elastic volumetric moduli K , which is calculated with initial elastic volumetric moduli K_0 , shear moduli G_0 and relevant model parameters m_s, m_f

$$p = K\varepsilon_v \quad K = K_0 p_a (p/p_a)^{m_v} \quad (\text{A.4})$$

$$q = 3G\varepsilon \quad G = G_0 p_a (p/p_a)^{m_s} \quad (\text{A.5})$$

In Equation (A.3), the following equation can be obtained from the elasto-plastic theory

$$[\mathbf{D}^e] \{d\varepsilon^e\} = \{d\sigma\} \quad \{d\varepsilon^p\} = d\lambda \{n_g\} \quad (\text{A.6})$$

Then, Equation (A.2) can be re-written as:

$$\{d\sigma\} = [\mathbf{D}^e] \{d\varepsilon\} - [\mathbf{D}^e] d\lambda \{n_g\} \quad (\text{A.7})$$

where $d\lambda$ is presented with a loading direction vector $\{n_f\}$ and plastic hardening modulus H

$$d\lambda = \frac{\{n_f\}^T \{d\sigma\}}{H} \quad (\text{A.8})$$

The preceding plastic flow direction vector $\{n_g\}$ loading direction vector $\{n_f\}$ in (p, q, θ) space can be calculated as:

$$\{n_g\} = (n_{gv}, n_{gs}, n_{g\theta})^T = \left(\frac{d_g}{\sqrt{1+d_g^2}}, \frac{1}{\sqrt{1+d_g^2}}, \frac{-qM_g \cos 3\theta}{2\sqrt{1+d_g^2}} \right)^T \quad (\text{A.9})$$

$$\{n_f\} = (n_{fv}, n_{fs}, n_{f\theta})^T = \left(\frac{d_f}{\sqrt{1+d_f^2}}, \frac{1}{\sqrt{1+d_f^2}}, \frac{-qM_f \cos 3\theta}{2\sqrt{1+d_f^2}} \right)^T \quad (\text{A.10})$$

where M_g denotes the slope of the critical state line, which is calculated by the angle of internal friction at the critical state and Lode's angle. M_f is the constitutive model parameter, when M_g equals M_f , the constitutive model obeys the associated flow rule.

Finally, the strain–stress can be expressed, and more details regarding the generalized elasto-plastic model can be found in the literature (Pastor et al., 1985, Liu et al., 2018, Zienkiewicz et al., 1985).

$$\{d\sigma\} = \left\{ [D^e] - \frac{[D^e]\{n_g\}\{n_t\}^T[D^e]}{H + \{n_t\}^T[D^e]\{n_g\}} \right\} \{d\varepsilon\} \quad (\text{A.11})$$

$$[D^{ep}] = [D^e] - \frac{[D^e]\{n_g\}\{n_t\}^T[D^e]}{H + \{n_t\}^T[D^e]\{n_g\}} \quad (\text{A.12})$$

Appendix B. Seismic wave input method

The vibration analysis method commonly used in earth rockfill dams disregards the inconsistency of ground vibration input and the effect of foundation radiation damping, whereas the seismic wave input method can effectively solve the above problems and more accurately simulate the interactions between the dam and foundation (Wong, 1982, Deeks and Randolph, 1994). Recently, a novel time-domain artificial boundary method Zhang et al. (2023a), Zhang et al. (2023b), called the scaled boundary perfectly matched layer (SBPML), was proposed to simulate radiation damps of infinite domain. In this method, a local modified scaled boundary coordinate system from the SBFEM is first introduced to describe the general geometric properties of the infinite domain.

In the two-dimensional problem, a four-node Goodman element without thickness is used to represent the viscoelastic boundary, and its normal and tangential spring coefficients k_n and k_t can be expressed as follows:

$$k_n = \alpha_n \frac{G}{r} \quad (\text{B.1})$$

$$c_n = \rho c_p \quad (\text{B.2})$$

$$k_t = \alpha_t \frac{G}{r} \quad (\text{B.3})$$

$$c_t = \rho c_s \quad (\text{B.4})$$

where c_n and c_t are normal and tangential damping coefficients of the viscoelastic boundary, c_p and c_s are the wave speeds of the P and S waves, α_n and α_t are constant, G represents the shear stiffness of the material at the viscoelastic boundary, ρ is the mass density, r is the distance from the seismic source to the boundary.

The general expression for the seismic equivalent load F_b is given by:

$$F_b = R_b + C_b \dot{u}_b + K_b u_b \quad (\text{B.5})$$

where R_b , u_b , \dot{u}_b are the force vector, displacement vector and velocity vector induced by the seismic wave at the viscoelastic boundary node. K_b and C_b are the stiffness and damping additional matrices of the boundary to the goodman element.

References

- Augarde, C.E., Lee, S.J., Loukidis, D., 2021. Numerical modelling of large deformation problems in geotechnical engineering: A state-of-the-art review. *Soils Found.* 61 (6), 1718–1735.
- Bandara, S., Ferrari, A., Laloui, L., 2016. Modelling landslides in unsaturated slopes subjected to rainfall infiltration using material point method. *Int J Numer Anal Met.* 40 (9), 1358–1380.
- Bardenhagen, S.G., 2002. Energy conservation error in the material point method for solid mechanics. *J Comput Phys.* 180 (1), 383–403.
- Bathe, K.J., Ramm, E., Wilson, E.L., 1975. Finite element formulations for large deformation dynamic analysis. *Int J Numer Meth Eng* 9 (2), 353–386.
- Belytschko, T., Lu, Y.Y., Gu, L., 1994. Element-free Galerkin methods. *Int J Numer Meth Eng.* 37 (2), 229–256.
- Benson, D.J., 1989. An efficient, accurate, simple ALE method for nonlinear finite element programs. *Comput Method Appl M.* 72 (3), 305–350.
- Boer, D.E., 1993. One-dimensional transient wave propagation in a fluid-saturated incompressible porous media. *Arch App Mech.* 63, 59–72.
- Chen, X.J., Fu, Y., Liu, Y., 2022. Random finite element analysis on uplift bearing capacity and failure mechanisms of square plate anchors in spatially variable clay. *Eng Geol.* 304, 106677.
- Chen, G., Yang, J., Wang, R., et al., 2023b. Seismic damage analysis due to near-fault multipulse ground motion. *Earthq Eng Struct D.*
- Chen, H., Zhao, S., Zhao, J., et al., 2023a. DEM-enriched contact approach for material point method. *Comput Method Appl M.* 404, 115814.
- Cuomo, S., Ghasemi, P., Martinelli, M., et al., 2019. Simulation of liquefaction and retrogressive slope failure in loose coarse-grained material. *Int J Geomech.* 19 (10), 04019116.
- Deeks, A.J., Randolph, M.F., 1994. Axisymmetric time-domain transmitting boundaries. *J Eng Mech.* 120 (1), 25–42.
- Di Carluccio, G., Pinyol, N.M., Alonso, E.E., et al., 2023. Liquefaction-induced flow-like landslides: the case of Valarties (Spain). *Géotechnique.* 1–18.
- Di, Y., Tang, X.W., 2007. Numerical simulation for large deformation dynamic problem in two-phase media. *Engineering Mechanics.* 24 (12), 47–52.
- Diebels, S., Ehlers, W., 1996. Dynamic analysis of a fully saturated porous medium accounting for geometrical and material non-linearities. *Int J Numer Meth Eng.* 39 (1), 81–97.
- Feng, K., Wang, G., Huang, D., et al., 2021. Material point method for large-deformation modeling of coseismic landslide and liquefaction-induced dam failure. *Soil Dyn Earthq Eng.* 150, 106907.
- Ghofrani, A., Arduino, P., 2018. Prediction of LEAP centrifuge test results using a pressure-dependent bounding surface constitutive model. *Soil Dyn Earth Eng.* 113, 758–770.

- Gibson, R.E., England, G.L., Hussey, M.J.L., 1967. The theory of one-dimensional consolidation of saturated clays: 1. finite non-linear consolidation of thin homogeneous layers. *Geotechnique* 17 (3), 261–273.
- J. Gong D. Zou X. Kong et al. A coupled meshless-SBFEM-FEM approach in simulating soil-structure interaction with cross-scale model *Soil Dyn Earth Eng* 2020,136: 106214.
- Gong, J., Zou, D., Kong, X., et al., 2021. An approach for simulating the interaction between soil and discontinuous structure with mixed interpolation interface. *Eng Struct* 237, 112035.
- Gong, J., Zou, D., Kong, X., et al., 2023. A meshfree large-deformation analysis method for geotechnical engineering based on the RBF field variable mapping technology. *Comput Method Appl M* 416, 116377.
- Gu, W.H., Morgenstern, N.R., Robertson, P.K., 1993. Progressive failure of lower San Fernando dam. *J Geotech Geoenviron* 119 (2), 333–349.
- Guo, N., Yang, Z., Yuan, W., et al., 2021. A coupled SPFEM/DEM approach for multiscale modeling of large-deformation geomechanical problems. *Int J Numer Anal Met* 45 (5), 648–667.
- Hatanaka, M., Uchida, A., Ohara, J., 1997. Liquefaction characteristics of a gravelly fill liquefied during the 1995 Hyogo-Ken Nanbu earthquake. *Soils Found* 37 (3), 107–115.
- Hosseinejad, F., Kalateh, F., Mojtahedi, A., 2019. Numerical Investigation of liquefaction in earth dams: A Comparison of Darcy and Non-Darcy flow models. *Comput Geotech* 116, 103182.
- Hu, Y., Randolph, M.F., 1998. A practical numerical approach for large deformation problems in soil. *Int J Numer Anal Met* 22 (5), 327–350.
- Huang, Y., Liang, H., Hideto, N., 2008. The state of the art of SPH method applied in geotechnical engineering. *Chinese J. Geotechnical Engineering* 30 (2), 256.
- Huang, Y., Xiong, M., 2017. Probability density evolution method for seismic liquefaction performance analysis of earth dam. *Earthq Eng Struct D* 46 (6), 925–943.
- Idelsohn, S.R., Oñate, E., Pin, F.D., 2004. The particle finite element method: a powerful tool to solve incompressible flows with free-surfaces and breaking waves. *Int J Numer Meth Eng* 61 (7), 964–989.
- Jie, Y., Tang, X., Luan, M., et al., 2008. Adaptive element free Galerkin method applied to analysis of earthquake induced liquefaction. *Earthq Eng Eng Vib* 7 (2), 217–224.
- Kafaji I K J. Formulation of a dynamic material point method (MPM) for geomechanical problems [M]. 2013.
- Kokkali, P., Abdoun, T., Zeghal, M., 2018. Physical modeling of soil liquefaction: Overview of LEAP production test 1 at Rensselaer Polytechnic Institute. *Soil Dyn Earth Eng* 113, 629–649.
- Li, W.L., Guo, N., Yang, Z.X., et al., 2021. Large-deformation geomechanical problems studied by a shear-transformation-zone model using the material point method. *Comput Geotech* 135, 104153.
- Liew, K.M., Ng, T.Y., Wu, Y.C., 2002. Meshfree method for large deformation analysis—a reproducing kernel particle approach. *Eng Struct* 24 (5), 543–551.
- Liu, Y., Chen, X., Hu, M., 2022. Three-dimensional large deformation modeling of landslides in spatially variable and strain-softening soils subjected to seismic loads. *Can Geotech J* 60 (4), 426–437.
- Liu, G.R., Gu, Y.T., 2001. A local point interpolation method for stress analysis of two-dimensional solids. *Struct Eng Mech* 11 (2), 221–236.
- Liu, G.R., Gu, Y.T., 2002. Comparisons of two meshfree local point interpolation methods for structural analyses. *Comput Mech* 29, 107–121.
- Liu, S., Tang, X., Luan, Y., et al., 2021. Seismic response analysis of subway station in deep loose sand using the ALE method. *Comput Geotech* 139, 104394.
- Liu, J., Zou, D., Kong, X., et al., 2018. A simple measurement of membrane penetration in gravel triaxial tests based on eliminating soil skeleton plastic deformation with cyclic confining pressure loading. *Geotech Test J* 42 (4), 880–896.
- Lombardi, D., Bhattacharya, S., 2014. Modal analysis of pile-supported structures during seismic liquefaction. *Earthq Eng Struct D* 43 (1), 119–138.
- Lucy, L.B., 1977. A numerical approach to the testing of the fission hypothesis. *Astrophys J* 82, 1013–1024.
- Manzari, M.T., El Ghorab, M., Kutter, B.L., et al., 2018. Liquefaction experiment and analysis projects (LEAP): Summary of observations from the planning phase. *Soil Dyn Earth Eng* 113, 714–743.
- Martinelli, M., Galavi, V., 2021. Investigation of the material point method in the simulation of cone penetration tests in dry sand. *Comput Geotech* 130, 103923.
- Martinelli, M., Galavi, V., 2022. An explicit coupled MPM formulation to simulate penetration problems in soils using quadrilateral elements. *Comput Geotech* 145, 104697.
- Menon, S., Song, X., 2023. Computational coupled large-deformation periporomechanics for dynamic failure and fracturing in variably saturated porous media. *Int J Numer Meth Eng* 124 (1), 80–118.
- Ming, H.Y., Li, X.S., 2003. Fully coupled analysis of failure and remediation of Lower San Fernando Dam. *J Geotech Geoenviron* 129 (4), 336–349.
- Moriwaki, Y., Beikae, M., Idriss, I.M., 1988. Nonlinear seismic analysis of the upper San Fernando Dam under the 1971 San Fernando Earthquake[C]. *Proc. 9th World Conf. on Earthquake Engineering*, Tokyo and Kyoto, Japan. 3, 237–241.
- Newmark, N.M., 1959. A method of computation for structural dynamics. *J. Eng. Mech. Div* 85 (3), 67–94.
- Noh, W.F.C.E.L., 1963. A time-dependent, two-space-dimensional, coupled Eulerian-Lagrange code. Lawrence Radiation Lab. Univ. of California, Livermore.
- Pastor, M., Zienkiewicz, O.C., Leung, K.H., 1985. Simple model for transient soil loading in earthquake analysis. II. Non-associative models for sands. *Int J Numer Anal Methods Geomech* 9, 477–498.
- Qu, Y., Zou, D., Kong, X., et al., 2020. Seismic cracking evolution for anti-seepage face slabs in concrete faced rockfill dams based on cohesive zone model in explicit SBFEM-FEM frame. *Soil Dyn Earth Eng* 133, 106106.
- Randolph M F, Wang D, Zhou H, et al. Large deformation finite element analysis for offshore applications[C]. *Proc., 12th Int. Conf. of the Int. Association for Computer Methods and Advances in Geomechanics*. Goa, India: IACMAG, 2008: 3307-3318.
- Reyes, A., Yang, M., Barrero, A.R., et al., 2021. Numerical modeling of soil liquefaction and lateral spreading using the SANISAND-Sf model in the LEAP experiments. *Soil Dyn Earth Eng* 143, 106613.
- Seed, H.B., 1973. Analysis of the slides in the San Fernando dams during the earthquake of Feb 9, 1971[M].
- Seed, H.B., Idriss, I.M., 1971. Simplified procedure for evaluating soil liquefaction potential. *J. the Soil Mechanics and Foundations division* 97 (9), 1249–1273.
- Seed, H.B., Lee, K.L., Idriss, I.M., et al., 1975. The slides in the San Fernando dams during the earthquake of February 9, 1971. *J. Geotech. Eng. Div* 101 (7), 651–688.
- Shahbodagh, B., Sadeghi, H., Kimoto, S., et al., 2020. Large deformation and failure analysis of river embankments subjected to seismic loading. *Acta Geotech* 15 (6), 1381–1408.
- Shantaram, D., Owen, D.R.J., Zienkiewicz, O.C., 1976. Dynamic transient behaviour of two-and three-dimensional structures including plasticity, large deformation effects and fluid interaction. *Earthq Eng Struct D* 4 (6), 561–578.
- Simon, B.R., Zienkiewicz, O.C., Paul, D.K., 1984. An analytical solution for the transient response of saturated porous elastic solid. *Int J Numer Meth Eng* 8 (4), 381–398.
- Sulsky, D., Chen, Z., Schreyer, H.L., 1994. A particle method for history-dependent materials. *Comput Method Appl M* 118 (1–2), 179–196.
- Talbot, L.E.D., Given, J., Tjung, E.Y.S., et al., 2024. Modeling large-deformation features of the Lower San Fernando dam failure with the material point method. *Comput Geotech* 165, 105881.
- Ullah, S.N., Hou, L.F., Satchithanathan, U., et al., 2018. A 3D RITSS approach for total stress and coupled-flow large deformation problems using ABAQUS. *Comput Geotech* 99, 203–215.
- Vasko, A., 2015. An investigation into the behavior of Ottawa sand through monotonic and cyclic shear tests. The George Washington University., Washington.
- Wang, D., Randolph, M.F., White, D.J., 2013. A dynamic large deformation finite element method based on mesh regeneration. *Comput Geotech* 54, 192–201.
- Wang, D., Bienen, B., Nazem, M., et al., 2015. Large deformation finite element analyses in geotechnical engineering. *Comput Geotech* 65, 104–114.
- Wong, H.L., 1982. Effect of surface topography on the diffraction of P, SV, and Rayleigh waves. *B Seismol Soc Am* 72 (4), 1167–1183.
- Wu, Q., Li, D.Q., Liu, Y., et al., 2021. Seismic performance of earth dams founded on liquefiable soil layer subjected to near-fault pulse-like ground motions. *Soil Dyn Earth Eng* 143, 106623.
- Xie, K.H., Leo, C.J., 2004. Analytical solutions of one-dimensional large strain consolidation of saturated and homogeneous clays. *Comput Geotech* 31 (4), 301–314.
- Ye, J., Wang, G., 2015. Seismic dynamics of offshore breakwater on liquefiable seabed foundation. *Soil Dyn Earthq Eng* 76, 86–99.
- Yerro, A., Soga, K., Bray, J., 2019. Runout evaluation of Oso landslide with the material point method. *Can Geotech J* 56 (9), 1304–1317.
- Yi, J.T., Liu, F., Zhang, T.B., et al., 2021. A large deformation finite element investigation of pile group installations with consideration of intervening consolidation. *Appl Ocean Res* 112, 102698.
- Yuan, W.H., Zhang, W., Dai, B., et al., 2019. Application of the particle finite element method for large deformation consolidation analysis. *Eng Computation* 36 (9), 3138–3163.
- Yuan, W.H., Liu, K., Zhang, W., et al., 2020. Dynamic modeling of large deformation slope failure using smoothed particle finite element method. *Landslides* 17, 1591–1603.
- Zhang, Y., Zhang, X., Nguyen, H., et al., 2023c. An implicit 3D nodal integration based PFEM (N-PFEM) of natural temporal stability for dynamic analysis of granular flow and landslide problem. *Comput Geotech* 159, 105434.
- Zhang, G., Zhao, M., Du, X., et al., 2023a. Time-domain scaled boundary perfectly matched layer for elastic wave propagation. *Int J Numer Meth Eng* 124 (18), 3906–3934.
- Zhang, G., Zhao, M., Zhang, J., et al., 2023b. Scaled Boundary Perfectly Matched Layer (SBPML): A novel 3D time-domain artificial boundary method for wave problem in general-shaped and heterogeneous infinite domain. *Comput Method Appl. M* 403, 115738.
- Zhao, S., Kang, F., Li, J., 2024. Intelligent segmentation method for blurred cracks and 3D mapping of width nephograms in concrete dams using UAV photogrammetry. *Automat Constr* 157, 105145.
- Zienkiewicz, O.C., Leung, K.H., Pastor, M., 1985. Simple model for transient soil loading in earthquake analysis. I. Basic model and its application. *Int J Numer Anal Met* 9 (5), 453–476.